Author Manuscript

Author Manuscript

Author Manuscript

Author Manuscript

HHS Public Access

Author manuscript

Cell Rep. Author manuscript; available in PMC 2022 May 02.

Published in final edited form as:

Cell Rep. 2022 March 22; 38(12): 110556. doi:10.1016/j.celrep.2022.110556.

Unique molecular features and cellular responses differentiate two populations of motor cortical layer 5b neurons in a preclinical model of ALS

Maria V. Moya[1], **Rachel D. Kim**[1], **Meghana N. Rao**[1], **Bianca A. Cotto**[1], **Sarah B. Pickett**[1], **Caroline E. Sferrazza**[1], **Nathaniel Heintz**[1,2], **Eric F. Schmidt**[1,3,*]

[1]Laboratory of Molecular Biology, The Rockefeller University, 1230 York Avenue, Box 260, New York, NY 10065, USA

[2]Howard Hughes Medical Institute, The Rockefeller University, New York, NY 10065, USA

[3]Lead contact

SUMMARY

Many neurodegenerative diseases, such as amyotrophic lateral sclerosis (ALS), lead to the selective degeneration of discrete cell types in the CNS despite the ubiquitous expression of many genes linked to disease. Therapeutic advancement depends on understanding the unique cellular adaptations that underlie pathology of vulnerable cells in the context of disease-causing mutations. Here, we employ bacTRAP molecular profiling to elucidate cell type-specific molecular responses of cortical upper motor neurons in a preclinical ALS model. Using two bacTRAP mouse lines that label distinct vulnerable or resilient projection neuron populations in motor cortex, we show that the regulation of oxidative phosphorylation (Oxphos) pathways is a common response in both cell types. However, differences in the baseline expression of genes involved in Oxphos and the handling of reactive oxygen species likely lead to the selective degeneration of the vulnerable cells. These results provide a framework to identify cell-type-specific processes in neurodegenerative disease.

Graphical Abstrct

This is an open access article under the CC BY-NC-ND license (http://creativecommons.org/licenses/by-nc-nd/4.0/).

*Correspondence: eschmidt@rockefeller.edu.

AUTHOR CONTRIBUTIONS

M.V.M, N.H., and E.F.S. conceived and designed the study. M.V.M., E.F.S., R.K., M.N.R., B.A.C., S.B.P., and C.E.S. performed all experiments. M.V.M. and E.F.S. analyzed data. M.V.M. and E.F.S. wrote the manuscript, with comments from B.A.C., R.K., and N.H.

SUPPLEMENTAL INFORMATION

Supplemental information can be found online at https://doi.org/10.1016/j.celrep.2022.110556.

DECLARATION OF INTERESTS

The authors declare no competing interests.

INCLUSION AND DIVERSITY

We worked to ensure sex balance in the selection of non-human subjects. One or more of the authors of this paper self-identifies as an underrepresented ethnic minority in science. One or more of the authors of this paper self-identifies as a member of the LGBTQ+ community. One or more of the authors of this paper self-identifies as living with a disability.

Author Manuscript Author Manuscript Author Manuscript Author Manuscript

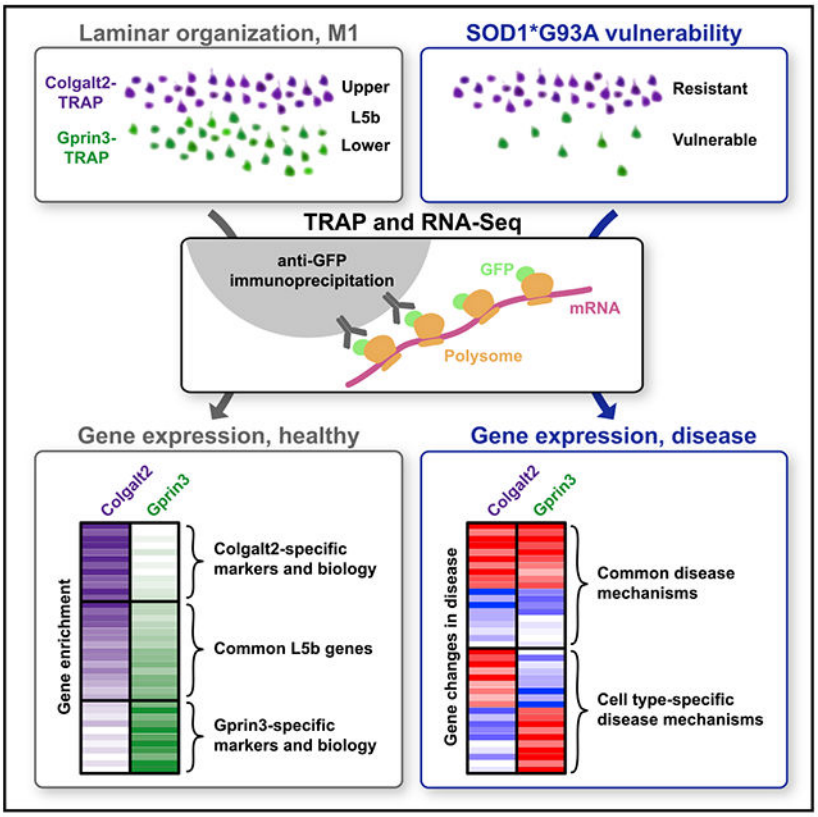

In brief

Moya et al. use bacTRAP mouse lines to characterize two highly related subpopulations of layer 5b projection neurons in motor cortex that are differentially susceptible to neurodegeneration in the SOD1-G93A mouse model of ALS. They identify the regulation of genes involved in bioenergetics as a key factor regulating susceptibility.

INTRODUCTION

Amyotrophic lateral sclerosis (ALS) is a fatal late-onset neurodegenerative disease that targets the motor pathways of the central nervous system and for which there is no cure. After symptom onset, the disease advances rapidly, with most patients experiencing progressive paralysis and eventual death within 2–5 years of diagnosis. Whereas most cases of ALS are sporadic, about 10% of cases are inherited (Rowland and Shneider, 2001; Tandan and Bradley, 1985). Gene linkage, genome-wide association studies (GWAS), and high-throughput sequencing studies have identified disease-causing mutations in over 50 genes, including *SOD1, C9ORF72, TARDBP, FUS, OPTN*, and *TBK1* (DeJesus-Hernandez et al., 2011; Kwiatkowski et al., 2009; Renton et al., 2011; Rosen et al., 1993; Sreedharan et al., 2008; Vance et al., 2009). Most ALS-linked genes are expressed widely throughout the brain and periphery and are involved in a variety of cellular pathways, including RNA processing, autophagy, membrane trafficking, and antioxidant function (Cook and Petrucelli, 2019). Despite their ubiquitous expression, mutations in these genes lead to specific loss

Author Manuscript Author Manuscript Author Manuscript Author Manuscript

of discrete cell populations, including the lower motor neurons in the brainstem and spinal cord and upper motor neurons in the motor cortex. This selective loss raises the question of which properties of motor neurons make them specifically vulnerable to ALS-causing mutations while other cells are seemingly resistant. Determining key cell type-specific biological contributors to cellular pathology and vulnerability will lay the groundwork for the discovery of more efficacious therapies.

Pathology and dysfunction of both lower and upper motor neurons is required for a diagnosis of ALS (Braak et al., 2013; Ravits et al., 2007). Most preclinical research has focused on lower motor neurons (see Ragagnin et al., 2019), since accessing the vulnerable cells in the forebrain and cortex is challenging due to the heterogeneity of cortical neuron types and a relative lack of reliable markers to distinguish among them. However, *post mortem* brains from patients with ALS show a loss of spinal-projecting Betz cells in layer 5 (L5) of the primary motor cortex (M1; Hammer et al., 1979) that is accompanied by vacuolization of apical dendrites (Genc et al., 2017; Saberi et al., 2015) and soma and axonal hyperexcitability (Eisen et al., 1996; Kohara et al., 1996; Vucic et al., 2013; Zanette et al., 2002). In preclinical rodent models, L5b corticospinal neurons in M1 show early hyperexcitability along with changes in dendritic structure and spine density (Fogarty et al., 2015; Kim et al., 2017; Saba et al., 2015). These are accompanied by corticospinal tract degeneration (Thomsen et al., 2014), dendritic vacuolization, and eventually death (Ozdinler et al., 2011; Yasvoina et al., 2013; Zang and Cheema, 2002). Many of these studies relied on acute labeling methods, such as retrograde tracing or transgenic animals, that broadly labeled excitatory L5b neurons. However, recent descriptions of axonal projection diversity and molecular heterogeneity within L5b necessitate that ALS pathology in these deep-layer neurons be assessed with greater cell type resolution.

Within the motor cortex, multiple subpopulations of L5b pyramidal tract-projecting (PT) neurons have been distinguished by their closely related but unique molecular profiles and axonal projection targets (Economo et al., 2016; Gerfen et al., 2018; Oswald et al., 2013; Tasic et al., 2016, 2018). To date, these L5b PT cell types have proved difficult to dissociate molecularly and anatomically in ALS mouse models, in part because of their close laminar proximity and similar morphological features. However, understanding the biological differences between these closely related PT neuron types can provide a unique opportunity to describe the specific features that may confer L5b neuron vulnerability in ALS and contribute to their pathology during disease progression.

Here, we utilized bacTRAP transgenic mice to target distinct populations of PT neurons in L5b of M1, including a subset that exhibits vulnerability to degeneration in the SOD1-G93A mouse model of ALS (Chiu et al., 1995; Gurney et al., 1994). We employed translating ribosome affinity purification (TRAP; Heiman et al., 2014; Heiman et al., 2008) to determine molecular features that distinguish these L5b cell types and may underlie differential vulnerability in disease. We show that only the Gprin3-TRAP-labeled corticospinal-projecting cells located in lower L5b (LL5b) degenerated in the SOD1-G93A mice, whereas upper-layer 5b (UL5b) pons-projection cells labeled in Colgalt2-TRAP mice were spared. Gprin3 cells exhibited a more robust molecular response to SOD1-G93A expression, including modulation of genes associated with maintenance of axon and synapse

Author Manuscript Author Manuscript Author Manuscript Author Manuscript

structure and function, while both resistant Colgalt2-TRAP cells and vulnerable Gprin3-TRAP cells increased their expression of oxidative phosphorylation (Oxphos) genes. Finally, we reveal that Gprin3 cells showed baseline differences in expression of oxidative stress and antioxidant response transcription factors, and that expression of these factors and their targets were further altered in SOD1-G93A mice.

RESULTS

Colgalt2-TRAP and Gprin3-TRAP cells occupy distinct sublayers of L5b in M1 cortex

We first set out to generate transgenic mouse lines to target PT neurons in L5b of M1. The GENSAT database (Gong et al., 2003) and the Allen Brain Atlas (Lein et al., 2007) were used to generate a list of candidate genes that showed selective expression in L5b pyramidal populations. Bacterial artificial chromosomes (BACs) were then used to generate bacTRAP mice expressing the EGFP-tagged ribosomal protein L10a (EGFP-L10a) under the control of these cell-type-specific promoters. Two of the candidate genes, *Colgalt2* and *Gprin3*, drove EGFP-L10a expression in pyramidal neurons across different regions of cortex, including the premotor and motor areas (Figures S1A-S1D). In the Colgalt2-bacTRAP line, EGFP-L10a expression was apparent across a broad medial-lateral (ML) and anterior-posterior (AP) extent across all cortical regions (Doyle et al., 2008; Groh et al., 2010; Schmidt et al., 2012). EGFP-L10a expression in the Gprin3-bacTRAP line was primarily restricted to rostromedial cortical areas, with few GFP+ pyramidal neurons detected posterior to bregma, lateral to sensory cortical areas, and medial to secondary motor cortex. GFP was also observed in a small subset of superficial-layer interneurons. Colgalt2 cells were rarely observed outside cortex, while Gprin3 cells were also detected in the hippocampus, the striatum, and other subcortical areas.

To confirm localization of Colgalt2 and Gprin3 cells in L5b, the depth of EGFP+ cells was measured relative to the pial surface (Figures 1A, 1B, S1E, and S1F). In M1, Colgalt2 cells were found in a narrow ~200-μm layer between ~40% and 65% from pial surface. They were located slightly deeper than S100a10 cells in L5a, suggesting that Colgalt2 cells were located in UL5b. Gprin3 cells were instead found at ~55%–75% depth and were located superficial to Ntsr1 cells in L6a, suggesting that Gprin3 cells reside in LL5b (Figure 1B). In primary sensory cortex (S1), Colgalt2 and Gprin3 cells were found at the same depth, ~50%–70% from the pial surface, indicating that the division of Colgalt2 and Gprin3 neurons into upper and lower sublayers is unique to motor areas. Both Colgalt2 and Gprin3 neurons displayed larger cell body size compared with other deep-layer neurons, including L5a S100a10, and L6a Ntsr1 cells (Figure 1C), as well as with other randomly selected pyramidal neurons across all cortical layers (Figure S1G). Immunofluorescent staining of tissue from each bacTRAP line revealed 79% of Colgalt2 and 94% of Gprin3 EGFP+ cells were co-labeled with CTIP2, a known marker of subcortical-projection neurons, confirming the PT identity of both populations (Figures 1D and S1H).

We next employed TRAP (Heiman et al., 2008, 2014) to examine the molecular profiles of each cell population more closely. EGFP-tagged polysomes containing the EGFP-L10a transgene were immunoprecipitated (IPed) from microdissected M1 homogenates from each bacTRAP line by using anti-EGFP antibodies. Polysome-bound mRNA was then isolated

Author Manuscript Author Manuscript Author Manuscript Author Manuscript

and subsequently processed for high-throughput RNA-seq. Relative to other cell types in the cortex and whole cortex input samples, UL5b Colgalt2 and LL5b Gprin3 cells clustered closely together by principal component analysis (PCA; Figure S2A), suggesting that although distinct, these two cell types likely share many molecular features. To determine the genes that were enriched across both Colgalt2 and Gprin3 cells, we performed differential expression (DE) analysis comparing TRAP mRNA from each cell type to mRNA purified from whole M1 (M1 input; Figure S2B). A total of 1,598 genes were significantly enriched (padj <0.05 and $\log_2$ fold enrichment[LFE]; LFE >0.5) in M1 Colgalt2 IPs, and 1,568 genes were significantly enriched in Gprin3 IPs (Figure S2B; Table S2). We found that 486 enriched genes were shared by both cell types, including known L5b marker genes *Fezf2, Crym, Nefh*, and *Serpine2*, whereas glial markers such as *Aif1*, *Gfap*, and *Mobp* were depleted (Figures 1E and 1F). Identification of genes specifically enriched within each cell type can serve as novel markers to distinguish these two PT cell types from each other and from other cell types in motor cortex without transgenic labeling. For example, *Vat1l* displayed high levels of enrichment in Colgalt2 cells, while *Lypd1* showed higher expression in Gprin3 cells (Figure 1F). Indeed, *in situ* hybridization (ISH) revealed that *Vat1l* transcripts specifically labeled GFP+ UL5b Colgalt2 cells, *Lypd1* was expressed specifically in GFP+ LL5b Gprin3 cells, and the pan-L5b marker *Nefh* labeled cells across both sublayers (Figure 1G). Together, these data show that Colgalt2 and Gprin3 neurons represent closely related but molecularly distinct populations of PT cells located across discrete sublayers of L5b.

Colgalt2 and Gprin3 cells share a PT projection to the pons, but Gprin3 cells alone project to more distal PT targets

CTIP2-positive pyramidal neurons located in L5b of M1 project to various subcortical areas and long-range PT targets, such as the spinal cord (Arlotta et al., 2005). To determine the axonal targets of M1 Colgalt2 and Gprin3 cells, we injected the retrograde tracer cholera toxin β subunit (CTB) into the pons, a proximal PT target (Figure 2A), and cervical (C6) spinal cord, a distal target (Figure 2C), of adult Colgalt2 and Gprin3 bacTRAP mice. In pons-injected animals, CTB+ neurons were localized to both UL5b and LL5b of M1 (Figures 2B and S3A) with laminar distributions 40%–75% from pia, overlapping with both Colgalt2 and Gprin3 cells (Figure 2E). In Colgalt2-bacTRAP mice, 64% of CTB+ cells in UL5b (and 38% of all CTB+ cells) were EGFP+ (Figure 2F), suggesting that Colgalt2 cells represent the majority of pons-projecting cells in UL5b. In Gprin3-bacTRAP animals, 77% of pontine CTB+ cells in LL5b (and 48% of all CTB+ cells) were co-labeled with EGFP, indicating that Gprin3 neurons represent LL5b cells that project to the pons (Figure 2F). These data also indicate that Colgalt2 and Gprin3 neurons represent the vast majority (~85%) of pons-projecting cells in M1 L5b.

In C6-injected animals, CTB+ cells were observed primarily in LL5b in M1, at a depth similar that of to Gprin3 neurons and distinctly deeper than Colgalt2 cells (~60%–75% from pia; Figures 2D, 2E, and S3A). In Gprin3-bacTRAP mice, 82% of spinal CTB+ cells were EGFP+, whereas only 9% of spinal CTB+ cells were EGFP+ in Colgalt2 bacTRAP mice (Figure 2F). We also observed CTB co-localization with Gprin3 cells when CTB was injected into brainstem motor nuclei 7N and 5N (Figures S3B-S3E). Together, these data reveal that the subcortical targets of EGFP+ neurons in Colgalt2-and Gprin3-bacTRAP mice

Author Manuscript Author Manuscript Author Manuscript Author Manuscript

are consistent with PT projections, and, while they both share a projection to the pons, the Gprin3 cells have distal collaterals that extend to the brainstem and cervical spinal cord.

Gprin3 cells are vulnerable to degeneration in SOD1-G93A mice, while Colgalt2 neurons are resistant

Because Gprin3 cells showed a projection to the spinal cord that Colgalt2 cells lacked, we hypothesized that Gprin3 cells would be vulnerable to degeneration in a mouse model of ALS. To determine vulnerability of Colgalt2 and Gprin3 cells in disease, we crossed Colgalt2 and Gprin3 bacTRAP mice to hSOD1-G93A (B6JL.SOD1-G93A$^{+/-}$) mice (Figure 3A), a widely used preclinical model of familial ALS (Chiu et al., 1995). SOD1-G93A-crossed mice began displaying tremors just after postnatal day 70 (P70), with severe deficits in rotarod performance appearing around 8 weeks of age (Figure S4A). Colgalt2-bac-TRAP:SOD1-G93A and Gprin3-bacTRAP:SOD1-G93A mice both reached end stage of disease at approximately P165, consistent with the typical survival time for this model (Figure S4B). We looked for signs of inflammation in M1 by staining for GFAP+-reactive astrocytes after P110 (Figure 3B). In wildtype (WT) animals, the majority of GFAP+ astrocytes were observed in deep L6 and in superficial L1 and L2/3 (Figures 3B and 3C). There was a marked increase in the number of GFAP+ astrocytes found in L5 of SOD1-G93A animals, between 40% and 75% depth from pia, suggesting the presence of dysfunction or degeneration in the vicinity of Colgalt2 and Gprin3 neurons.

We next wanted to determine whether UL5b Colgalt2 or LL5b Gprin3 cells in M1 degenerate in SOD1-G93A animals. We counted the number of EGFP+ cells in serial coronal sections of M1 from Colgalt2-bacTRAP and Gprin3-bacTRAP mice expressing SOD1-G93A (SOD) or WT littermates to assess changes in cell number along the AP axis. Cells were counted across early (P70) and late (P110) symptomatic time points. We found no change in the number of Colgalt2 neurons along the extent of M1 (bregma +1.00 to 0.00 mm) in SOD1-G93A mice at either age (Figures 3D and 3E). Whereas there was no difference in the number of Gprin3 neurons at P70, there was a significant decrease in the number of Gprin3 neurons in M1 at P110 (Figures 3D and S4C), with the greatest proportional loss found at more posterior coordinates (44% loss at bregma +0.50 mm, and 55% at bregma +0.25 mm; Figure 3F). The loss of Gprin3 neurons but not Colgalt2 neurons in SOD1-G93A mice reinforces the cell type specificity of vulnerability even between closely related UL5b PT cells and underscores the value of the Gprin3 and Colgalt2 bacTRAP lines to provide reproducible access to vulnerable and resilient populations, respectively.

Vulnerable Gprin3 cells showed a robust molecular response to SOD1-G93A mutation

The vulnerability of LL5b Gprin3 cells and resistance of UL5b Colgalt2 cells in SOD1-G93A mice presented a unique opportunity to measure cell-type-specific molecular responses of two closely related L5b populations during disease. We performed TRAP on M1 from SOD1-G93A mice (SOD) and healthy littermates (WT) for both Colgalt2 and Gprin3 bacTRAP lines at P110 and analyzed polysome-bound transcripts by RNA-seq. WT and SOD samples from both Colgalt2 and Gprin3 IPs were enriched for classic PT cell type genes and depleted for glial markers relative to input, confirming cell type specificity

Author Manuscript Author Manuscript Author Manuscript Author Manuscript

of TRAP isolations (Figure 4A). Importantly, SOD1-G93A expression did not significantly alter the relative expression of these markers in either cell type. Mapping TRAP-seq reads to the human *SOD1* gene showed the mutant *SOD1* transgene was expressed at similar levels in each cell type (Figure S5D).

We next identified genes that showed a significant change in expression in disease by performing DE analysis between WT and SOD samples (Table S3). DE revealed that only 17 genes were significantly regulated (padj <0.05 and baseMean >100 $\log_{10}$CPM) in M1 whole tissue (input) samples in response to SOD1-G93A expression (Figures 4B and S5A). Resistant Colgalt2 cells instead showed 120 genes with significant changes in expression in disease, with 114 up-regulated and six down-regulated genes in the SOD condition (Figures 4B and S5A). Vulnerable Gprin3 cells, in contrast, showed the most robust response to SOD1-G93A expression, with 1,654 genes differentially regulated (705 up-regulated and 949 down-regulated). Comparing the fold change in disease for each gene across the two cell types identified 61 genes significantly up-regulated in both cell types and only three that were commonly down-regulated (Figures 4C and S5B). Gene ontology (GO) analyses on DE genes from Colgalt2 or Gprin3 cells revealed genes related to Oxphos were up-regulated in both cell types, while Gprin3 cells additionally up-regulated genes associated with translation and mitophagy (Figures 4D, 4E, and S5C). Genes associated with regulation and maintenance of neuronal processes, i.e., axons, dendrites, and synapses, were down-regulated in Gprin3 cells (Figures 4E and S6A). These analyses revealed that vulnerable Gprin3 cells had a relatively robust molecular response to SOD1-G93A, and they highlight common and cell type-specific molecular changes that occur in response to SOD1-G93A expression in PT cells.

Identification of cell-type-specific molecular responses to SOD1-G93A

To explore in more detail the relative specificity of the molecular responses of vulnerable Gprin3 and resistant Colgalt2 cells in SOD1-G93A mice, we examined changes in expression of the individual genes that compose the altered functional pathways. Synaptic and axonal genes significantly decreased by 50% in Gprin3 cells in SOD animals compared with WT but showed no change in M1 inputs and a very small decrease in Colgalt2 TRAP data (Figures 5A and 5B). Because “cytoplasmic translation” was up-regulated with disease in Gprin3 cells (Figure 4E), we looked at ribosomal genes across both cell types. Surprisingly, nearly all small and large ribosomal subunit genes were increased in both Gprin3 and Colgalt2 cells, although the change in Gprin3 cells (~1.5-fold increase) was significantly greater relative to Colgalt2 cells (~1.3-fold; Figures 5C and 5E). Genes encoding mitochondrial ribosome subunits were also increased in both cell types, again with a significantly larger (~1.4-fold) increase in Gprin3 cells compared tothan in Colgalt2 (~1.3-fold; Figures 5D and 5E). There was no change in cytosolic or mitochondrial ribosome genes in M1 input, suggesting that this may be an adaptation specific to PT cells in response to SOD1-G93A. Additionally, these data reveal that the pathways selectively regulated in Gprin3 cells, such as synaptic and axonal structure and function, may underlie upper motor neuron-specific pathology in the disease and contribute to selective loss of these vulnerable cells.

Author Manuscript Author Manuscript Author Manuscript Author Manuscript

Oxphos genes were up-regulated across both resistant Colgalt2 and vulnerable Gprin3 cells but showed differential baseline levels of expression between these two cell types

One set of genes that showed a significant up-regulation by DE in both Colgalt2 and Gprin3 cells belonged to the Oxphos pathway (Figures 4C and 4D). This increase suggested that a change in bioenergetic demand and respiration may be a default response to SOD1-G93A expression in L5b cells. To determine whether this up-regulation of Oxphos genes included all complexes of the electron transport chain (ETC) or was selective to specific subunits, we compared the relative expression level of each gene composing the individual complexes (Figure 6A). We found that Colgalt2 and Gprin3 cells showed a significant ~1.4-fold up-regulation of all functional complexes in SOD, which was not detectable in M1 input samples (Figures 6B, S6B, and S6C). We also noted a small but non-significant up-regulation of genes that compose the tri-carboxylic acid cycle (TCA) in both Colgalt2 and Gprin3 cells in disease and no changes in genes coding for the glycolysis pathway (Figures 6B and S6B), suggesting that whereas aerobic metabolism may be increased in disease, anaerobic metabolism does not appear to be modulated. Gprin3 cells exhibited a unique 1.3-fold up-regulation of genes involved in mitochondrial transmembrane transport and a 1.6-fold increase in a subset of mitochondrial autophagy genes in SOD animals, whereas Colgalt2 cells had only a significantly smaller 1.2-fold increase in mitophapy genes (Figures 6B and S6B). This suggests that while an increase in respiration may be a common response to SOD1-G93A expression across L5b cells, certain important mitochondria-associated mechanisms are more strongly modulated only in vulnerable LL5b cells.

While both Colgalt2 and Gprin3 cells exhibited a significant up-regulation in Oxphos-related genes in SOD1-G93A mice, these genes were expressed at higher levels in WT Gprin3 cells compared with WT Colgalt2 cells (Figures 6A, S6B, and S6C). This was also seen in the baseline TRAP data, not crossed to the SOD1-93A mice (Figures 1E and S2B). Gprin3 cells had a median 1.75-fold higher level of Oxphos gene expression than Colgalt2 cells (Figure 6C) and oxidative phosphorylation was the most enriched GO category in Gprin3 DE genes compared with both M1 input and Colgalt2 cells (Figures S2C-S2E). This suggests that Gprin3 cells not only increase their levels of Oxphos gene expression in response to SOD1-G93A but that they inherently express these genes at higher levels compared with Colgalt2 neurons and other cortical cell types. Consistent with this, pyramidal cells in LL5b showed increased COX6C labeling but no difference in gross mitochondrial morphology compared with UL5b cells (Figures S7A-S7D). However, we did not detect significant changes in gross mitochondrial morphology in UL5b or LL5b cells in SOD1-G93A mice (Figures S7E-S7H).

Expression of a hypoxia- and antioxidant-responsive transcriptional program underlies cell-type-specific changes in vulnerable Gprin3 cells

We hypothesized that a disease-related increase in Oxphos output over the already elevated level of respiration in Gprin3 cells at baseline could lead to a corresponding increase in production of reactive oxygen species (ROS) and cell stress (Figure 7A). We therefore examined the TRAP data to see if the expression of genes in oxidative stress response (OSR) pathways were significantly modulated in L5b cells in SOD1-G93A mice. In Gprin3

Author Manuscript Author Manuscript Author Manuscript Author Manuscript

cells, 45 OSR genes were significantly changed in disease, with 20 being increased and 25 decreased (Figure 7B). Similar changes were not observed in the whole-tissue M1 input samples, and only four of these genes, *Ndufa12, Romo1, Selenok*, and *Sod1*, were up-regulated in Colgalt2 cells. Notably, nine of the down-regulated genes in Gprin3 cells, including *Hif1a, Epas1*, and *Nfe2l2*, code for transcription factors important for controlling cellular responses to hypoxia and ROS (Hamanaka and Chandel, 2009; Kobayashi et al., 2009; Semenza, 2001). Examination of the relative expression of these and other hypoxia and OSR factors across baseline Gprin3 and Colgalt2 data revealed that Gprin3 cells innately expressed lower levels of the factors *Foxo1, Epas1, Nfe2l2*, and *Notch1* compared with Colgalt2 cells and M1 input (Figures 7C and S8B), with *Epas1* and *Notch1* showing ~11.5- and 4.5-fold enrichment in Colgalt2 cells over Gprin3 cells, respectively. Together, these data highlight cell-type-specific discrepancies in handling ROS-reactive factors and suggest that lower baseline expression of OSR transcriptional programs, compounded with a further down-regulation during disease, may have severe consequences for the ability of Gprin3 cells to manage increased ROS production in the presences of SOD1-G93A.

DISCUSSION

The selective vulnerability of corticospinal L5b PT neurons in M1 to ALS-causing mutations has been described across species (Hammer et al., 1979; Ozdinler et al., 2011; Thomsen et al., 2014; Zang and Cheema, 2002), although the mechanisms that underlie their degeneration compared with other L5b cell types have remained elusive. Our results demonstrate that, while there is overlap in the cellular adaptations by vulnerable and resilient L5b populations to an ALS-causing mutation, the intrinsic properties of each cell type dictate how they respond to these adaptations to determine survival or degeneration, thus providing a molecular definition of vulnerability to disease.

M1 is important for motor planning, learning, and execution and is widely connected throughout the CNS through the longdistance projections of L5b PT cells (Gu et al., 2017; Guo et al., 2015; Kawai et al., 2015; Suter et al., 2013). Within M1, Colgalt2 and Gprin3 cells represent molecularly distinct subtypes of L5b PT neurons that are distributed into UL5b and LL5b, respectively, but both converge into the same layer in other regions of cortex. This is consistent with the variation of the thickness of cortical laminae across different functional areas, including an expansion of L5b in the motor regions of cortex (Caviness, 1975; Cederquist et al., 2013) where local intracortical afferents vary between upper and lower subdivisions of L5b (Hooks et al., 2013). Additionally, the divergence of axonal projections of Colgalt2 and Gprin3 cells implies unique roles for each cell type in motor output and corresponds to the distinct projection patterns of UL5b and LL5b in ALM (Economo et al., 2018). Previously generated transgenic mouse lines that target L5b, such as the commonly used Thy1-EYFP line (Bareyre et al., 2005; Feng et al., 2000; Yu et al., 2008) and Uchl1-EGFP line (Yasvoina et al., 2013), show expression of reporters and constructs across all of L5b rather than in its distinct sublayers. Therefore, the Gprin3 and Colgalt2 bacTRAP mouse lines enable reproducible molecular and anatomic access to two closely related L5b PT subtypes that were differentially vulnerable to disease.

Author Manuscript Author Manuscript Author Manuscript Author Manuscript

TRAP profiling revealed significant molecular adaptations in both L5b populations in symptomatic SOD1-G93A mice. While the response was more robust in the vulnerable Gprin3 cells, a number of shared changes were observed to a lesser degree in Colgalt2 neurons, highlighting a commonality of cellular responses to SOD1-G93A expression in both PT cell types. Most notably, both cells exhibited an up-regulation of mitochondrial genes, specifically those involved in Oxphos pathways. Studies from human patients and animal models have shown that mitochondrial dysfunction is a common, early phenomenon in ALS and other neurodegenerative diseases. Mitochondria are the primary site for the generation of ATP through Oxphos—accounting for 90% of all ATP generated in the CNS (Hyder et al., 2013)—and, as a byproduct, are the major source of ROS (Adam-Vizi and Chinopoulos, 2006; Hirst et al., 2008; Kudin et al., 2004; Lenaz et al., 2002; Muller et al., 2004; Nunnari and Suomalainen, 2012). The appearance of deficits in Oxphos, mitochondrial calcium buffering, generation of ROS, and mitochondrial transport have been observed prior to the onset of ALS symptoms (Bowling et al., 1993; Browne et al., 2006; Jaiswal, 2014; Sasaki et al., 2005), and aggregation of mutant SOD1 within mitochondria leads to free radical generation, ETC disruption, loss of mitochondrial membrane potential, diminished Oxphos, and decreased ATP production (Mattiazzi et al., 2002; Vandoorne et al., 2018). While most evidence for altered mitochondrial function has come from spinal cord or cultured motor neurons, high-throughput sequencing of frontal cortex from patients with sporadic or *C9ORF72*-linked ALS found dysregulation of Oxphos genes in both cases (Prudencio et al., 2015). Oxidative stress, including an up-regulation of Oxphos, was also a defining feature of a subset of motor cortex samples from a separate cohort of patients with ALS (Tam et al., 2019). The modulation of aerobic metabolism is likely a specific adaptation of L5b PT cells rather than a global response to disease-causing mutations, since we did not detect any changes in whole tissue input samples.

Gprin3 cells exhibited adaptations indicative of cellular stress and neurodegenerative mechanisms, including an up-regulation of genes associated with mitophagy, that were not seen in the resilient Colgalt2 population. The selective removal of dysfunctional mitochondria through mitophagy is a key strategy for mitigating cellular stress and can be used to delay the initiation of cell death (Green et al., 2011; Twig and Shirihai, 2011). Prompt removal of damaged mitochondria is critical for cell viability and the energy demands of neurons. Inefficient turnover of mitochondria by ALS-associated mutations in *TBK1* and *OPTN* genes implies a potential role for impaired mitophagy in ALS (Evans and Holzbaur, 2019; Moore and Holzbaur, 2016; Wong and Holzbaur, 2014). An increase in mitophagic gene expression likely reflects a pro-survival adaptation in Gprin3 cells at the symptomatic stage. Gprin3 cells also down-regulated genes involved in maintaining synaptic and axonal structure and function, signifying morphological changes associated with dysfunction and cell death. Degeneration of corticospinal axons is a hallmark of ALS, and L5b neurons in M1 undergo dendritic and synaptic atrophy at a pre-symptomatic age (Fogarty et al., 2015; Saba et al., 2015), which may include a down-regulation of synaptic genes (Kim et al., 2017). Our findings suggest that these changes may persist beyond this pre-symptomatic stage and are most robust in the vulnerable corticospinal subpopulation of L5b neurons.

Author Manuscript Author Manuscript Author Manuscript Author Manuscript

The neurodegeneration of Gprin3 cells and resilience of Colgalt2 cells to SOD1-G93A expression, despite their substantial overlap in molecular adaptations in symptomatic animals, raises the possibility that the inherent molecular properties of these cells drive divergent consequences in disease. In healthy animals, Gprin3 cells had higher baseline levels of Oxphos gene expression than Colgalt2 cells and total M1 tissue. This suggests that Gprin3 neurons may have increased bioenergetic needs compared with other neurons in M1. Computer modeling has predicted that the higher energy demands of large neurons, such as fast fatigable spinal motor neurons, made them more sensitive to changes in ATP availability that may occur in neurodegenerative diseases such as ALS (Le Masson et al., 2014). Indeed, greater vulnerability appears to positively correlate with cell size in spinal cord (Pun et al., 2006; Robberecht and Philips, 2013), with vulnerable alpha motor neurons having larger soma size, axon diameter, more dendritic branching, and greater innervation fields compared with ALS-resilient alpha motor neurons or gamma motor neurons (Ragagnin et al., 2019; Shoenfeld et al., 2014). This concept is further demonstrated in a model of spinal muscular atrophy (SMA), where selective vulnerability arose from alterations of the basal bioenergetic profile of distinct motor neuron pools and were rescued by manipulation mitochondrial or non-mitochondrial bioenergetic pathways (Boyd et al., 2017). Our data suggest that this may be true for subclasses of cortical neurons in ALS as well, necessitating closer examination of mitochondrial function in these cells.

Cellular respiration rates have been shown to decrease in ALS even before pathologies develop (Browne et al., 2006; Cozzolino and Carri, 2012; Irvin et al., 2015; Kawamata and Manfredi, 2010; Peixoto et al., 2013). Therefore, the increased expression of Oxphos genes by L5b cells may act as a compensatory mechanism to restabilize homeostasis. One possible explanation for the selective vulnerability of Gprin3 cells may be that, despite the increased Oxphos, they are poorly equipped to handle the subsequent changes in the balance of ROS as implied by the decrease in the expression of transcription factors downstream of mitochondrial ROS. These factors are critical regulators of the cell's response to toxic ROS (Hamanaka and Chandel, 2009; Kobayashi et al., 2009), and their deletion leads to numerous cellular pathologies (Lee et al., 2003a, 2003b; Scortegagna et al., 2003). This phenomenon has been demonstrated in cerebellar granule cells and hippocampal CA1 neurons, which are both inherently sensitive to oxidative damage (Wang and Michaelis, 2010; Wang et al., 2009). Hence, it is possible that, similar to other oxidative stress-sensitive neurons, an inherently high baseline of ROS may make Gprin3 cells more vulnerable to further increases in ROS production, and in a situation where the cells enter a state of acute oxidative stress or hypoxia, Gprin3 cells may be slower to respond than neighboring cells. Future work should test more directly how baseline differences in the OSR affect the sensitivity of L5b subtypes to ALS-causing mutations.

Mitochondrial pathology, such as vacuolization, has been reported in the CNS of transgenic of mice expressing high levels of WT human *SOD1* (Jaarsma et al., 2000). Since this was also observed in spinal motor neurons of SOD1 mutants that retained dismutase activity (such as G93A) but not in those where dismutase activity was disrupted (Bergemalm et al., 2006), we cannot rule out the possibility that the changes in mitochondrial genes in the bacTRAP mice were a general response to elevated dismutase activity and not related to disease. However, the mitochondrial abnormalities from WT *SOD1* overexpression were

Author Manuscript Author Manuscript Author Manuscript Author Manuscript

observed in much older animals (>30 weeks) than used in the current study (~16 weeks), and only minimal irregularities were observed in cortex even after 40 weeks (Jaarsma et al., 2000). When considered alongside a previous study that showed upper motor neurons were spared in WT *SOD1*-overexpressing mice (Ozdinler et al., 2011) and a lack of changes in mitochondrial-related genes in our whole tissue samples, our results likely reflect pathological mechanisms arising from the mutant transgene and not a generalized response to SOD1 overexpression. However, further molecular profiling experiments comparing WT and mutant *SOD1* overexpression in both UL5b and LL5b neurons will more definitively tease apart these possibilities.

By comparing two highly related yet distinct L5b projection neuron populations that have differential vulnerability to degeneration in a preclinical ALS model, we show that a defining feature of a vulnerable population is an elevated expression of genes involved in energy production and that a further up-regulation of this pathway is a key molecular signature for cellular responses to disease. This is an example of a specific, intrinsic cellular property of a vulnerable population that is also uniquely, and directly, altered by disease pathology in ALS. Further studies are needed to flesh out the link between cell type-specific differences in the expression of nuclear encoded mitochondrial genes, energetic output, and neurodegeneration.

Limitations of the study

In this study, we utilized two transgenic bacTRAP mouse lines for anatomic and molecular characterization of upper and lower L5b PT neurons in M1 of healthy animals and a preclinical ALS model. However, two important caveats must be considered. First, the TRAP-expressing neurons in these lines account for approximately 70%–80% of PT cells in the motor cortex. Currently, we do not know whether the 20%–30% of remaining cells represent separate PT types or an incomplete penetrance of the transgene within the population. It is possible that the unlabeled PT cells have distinct molecular responses to SOD1-G93A that were not represented in our TRAP data. Nevertheless, we demonstrate that Gprin3 cells undergo ALS-related degeneration; therefore, our data reflect pathological mechanisms within a majority of the vulnerable cells. Second, it is important to bear in mind that ALS is a progressive disease with variability in the onset of neurodegeneration even within vulnerable cell types. Such heterogeneity in the TRAP data could lead to a masking of some disease-relevant pathways or some representation of healthy cells. Since we uncovered dysregulation of pathways linked to ALS-related degeneration in the Gprin3 cells, we feel confident that our data reveal the most robust molecular responses across the population as a consequence of disease. Regardless, the heterogeneous nature of progression may be better teased apart in future studies utilizing single-cell transcriptomics.

STAR★METHODS

RESOURCE AVAILABILITY

Lead contact—Further information and requests for resources should be directed to and will be fulfilled by the lead contact, Eric F. Schmidt (eschmidt@rockefeller.edu).

Author Manuscript Author Manuscript Author Manuscript Author Manuscript

Materials availability

- The Gprin3-bacTRAP mouse line is currently available for distribution upon request with the completion of a Material Transfer Agreement (MTA). We are in the process of depositing this line to The Jackson Laboratory (JAX) and an official strain name and catalog number are pending.
- Plasmids generated in this study are currently available upon request and are in the process of being deposited to Addgene (catalog # pending).

Data and code availability

- The RNA-seq data from TRAP experiments have been deposited at the NCBI Gene Expression Omnibus (GEO) and are publicly available as of the date of publication. The accession number (GSE172484) is listed in the key resources table.
- All original code generated for this study have been deposited at Zenodo and are publicly available at https://zenodo.org/badge/latestdoi/374798433.
- Any additional information required to reanalyze the data reported in this paper is available from the lead contact upon request.

EXPERIMENTAL MODEL AND SUBJECT DETAILS

Animals—All animal procedures and experiments were done in accordance with The Rockefeller University Institutional Animal Care and Use Committee (IACUC) with National Institutes of Health (NIH) policies and guidelines. Eight-to-twelve-week-old mice were used for all baseline TRAP, retrograde labeling, histology, and RNAscope experiments. For experiments with SOD1*G93A mice, tissue was collected from 9-week old animals for the pre-symptomatic time point and 16-week-old animals for symptomatic time point.

Colgalt2-bacTRAP mice (Jackson Laboratory stock #030257, RRID:IMSR_JAX:030257) and Gprin3-bacTRAP mice (Eric Schmidt, The Rockefeller University) were used, and crossed with C57Bl/6J mice (Jackson Laboratory stock #000664, RRID:IMSR_JAX:000664) or SOD1*G93A mice (Jackson Laboratory Stock #004435, RRID:IMSR_JAX:004435). For mitochondrial morphology experiments, Gng7-Cre mice (GENSAT, The Rockefeller University, RRID:MMRRC_031180-UCD) were additionally used. For disease characterizations, SOD1*G93A$^{-/-}$ littermates were used as controls for SOD1*G93A$^{+/-}$ mice.SOD1*G93A$^{+/-}$ animals that were no longer able to freely move or feed were promptly euthanized in accordance with IACUC guidelines. Both male and female mice were used equally in this study. Animals were group housed in a 12hr/12hr light-dark cycle environment and were provided ad libitum access to food and water.

To generate the Gprin3-bacTRAP line, a sequence homology arm corresponding to the region upstream of the ATG start codon of Gprin3 was cloned into the pS296 targeting vector containing EGFP-L10a (Heiman et al., 2008). Recombination was performed by electroporating the modified pS296 vector into competent DH10β bacteria containing a pSV1.RecA plasmid and the RP24-127P5 BAC. The modified BAC was isolated and microinjected into the pronuclei of fertilized FVB/N mouse oocytes at 0.5 ng/μL. Transgenic

Author Manuscript Author Manuscript Author Manuscript Author Manuscript

founder mice were generated and crossed to C57BL/6J mice. F1 progeny were screened for proper transgene expression by EGFP genotyping and immunohistochemistry using expression in L5b was as a benchmark. Founder line ES152 was selected for expansion.

METHOD DETAILS

Cloning of viral constructs for mitochondrial labeling—The MitoGFP construct was acquired from the pLYS1-FLAG-MitoGFP-HA plasmid, as a gift from Vamsi Mootha (Addgene: 50057; RRID:Addgene_50057). The coding region was cloned into a Cre-dependent DIO pAAV plasmid (Nectow et al., 2017) by adding plasmid sequence homology to the MitoGFP insert at its 5′ and 3′ ends. The virus was then packaged into AAV2/9 by UPenn Viral Vector core. The mCherry-TOMM20 construct was also acquired from the mCherry-TOMM20-N-10 plasmid, as a gift from Michael Davidson (Addgene: 55146; RRID:Addgene_55146), and was cloned by homologous recombination into a non-Cre-dependent version of the above pAAV plasmid for constitutive expression. The construct was packaged into the “SL1” virus in collaboration with the Janelia Research Campus Viral Core.

Rotarod—SOD1*G93A mice and wildtype littermates (WT) were trained on the apparatus for three days beginning at five weeks of age (about postnatal day 35, ~P35) and then tested once weekly for six weeks. During the test, acceleration was increased from 5-18 rpm over the course of 180 seconds and the latency to fall was measured for two trials. Falls were detected automatically by a sensor at the base of the apparatus.

Retrograde anatomical tracing—Animals were anesthetized via IP injection of 1% Ketamine/0.1% Xylazine (doses 1 mL/kg and 0.1 mL/kg respectively) in 0.9% saline. Following anesthesia, animals were positioned on the stereotaxic apparatus, and skin and periosteum were incised above the skull. Pons injections were made at AP −4.1 mm, ML +/−0.6 mm, DV −5.2 mm. Holes were drilled in the skull at the target coordinates using a dental drill. Cholera toxin beta (Alexa 555-conjugated CTB, Thermo Fisher) was injected using a Hamilton syringe with a pulled glass capillary pipette at a rate of 0.1 μL/min to a total volume of 0.25 μL. Incisions were closed using Vetbond (3M). For spinal cord injections, an incision was made from the base of the neck down between the shoulder blades to target the cervical vertebrae. Back and shoulder muscles were separated by cutting connective ligaments with a scalpel. Once the spinal column was exposed, connective tissue was pushed aside slowly using the scalpel blade. Using forceps and surgical scissors, the C6 vertebrae was cut away to reveal the dura and spinal tissue. After carefully cutting a hole in the dura using forceps and scalpel, CTB was injected at a rate of 0.1 μL/min to a total of 0.15–0.20 μL at the following coordinates: AP C6 vertebra, ML +/−0.4 mm, DV −1.1 mm. Sutures were used to reposition back and shoulder muscles before suturing the incision. Animals were allowed to recover in clean cages over a warming plate and were given low dose ibuprofen in drinking water during recovery. Animals were perfused after at least 48 hrs following surgery to allow tracer to fully travel the length of the axons.

Virus injections—Adult animals were anesthetized via IP injection of 1% Ketamine/0.1% Xylazine (doses 1 mL/kg and 0.1 mL/kg respectively) in 0.9% saline. Mice were then

Author Manuscript Author Manuscript Author Manuscript Author Manuscript

head-fixed into stereotaxic apparatus, and the scalp was resected before drilling small bores over target injection sites. AAV9.Ef1a.DIO.MitoGFP or SL1.Ef1a.mCherry.TOMM20 was injected at a rate of 0.1 μL/min to a total of 0.15–0.25 μL into the pons of Gng7-Cre (for MitoGFP) and wildtype C57 or SOD1*G93A mice (for mCherry.TOMM20) via angled injection to AP −4.15, ML +/−2.01, DV −5.05, 15° from vertical. After suturing was completed, mice were allowed to recover in clean cages over a warming plate, and were given low dose ibuprofen in drinking water for up to one week following the surgery. Viral expression was allowed to continue for 4–5 weeks before collecting tissues, with periodic health checks performed during this time. Mice injected with SL1.Ef1a.mCherry.TOMM20 were injected at a pre-symptomatic age of 8 weeks so as to allow expression levels to plateau around the symptomatic disease stage.

Tissue collection and histology—Brain and spinal cord tissue were collected from experimental mice following cardiac perfusion. Mice received an IP injection of 1% Ketamine/0.1%Xylazine (lethal doses 2 mL/kg and 0.2 mL/kg respectively). Mice were perfused first with approximately 40 mL of sterile phosphate buffered saline (PBS) pH 7.4, followed by approximately 30 mL of freshly made 4% paraformaldehyde in PBS. Brain and spinal cord were removed and placed in 4% paraformaldehyde overnight at 4°C with shaking. Tissues were then transferred to 30% w/v sucrose in PBS and stored at 4°C for approximately 2 days. Brain and spinal cord tissues were sectioned on a sliding freezing microtome at a thickness of 40 μm. To section spinal cord tissue on the microtome, tissue was first embedded in Neg 50 (Thermo Fisher) or OCT medium (Tissue-Tek). Sections were stored in non-freezing storage media (25% w/v ethylene glycol, 25% glycerol, 50% PBS) at −20°C until further processing. Before staining or mounting, sections were washed 3 x 5 min with PBS.

Immunostaining—All fluorescent antibody staining experiments were performed on 40 μm free-floating tissue sections as follows: sections were washed in PBS pH 7.4, 3 x 5 min to remove anti-freezing storage solution. They were then incubated with 2.5% Normal Donkey serum (NDS, Jackson Immuno) with 2.5% TritonX-100 in PBS for approximately 30 mins, followed by 1% NDS, 1% TritonX-100, and primary antibodies in PBS overnight at room temperature with shaking. Sections were washed with PBS 3 x 5 min before incubating in 1% NDS with fluorescent secondary antibodies in PBS for approximately 1 hour. Sections were washed with PBS 3 x 5 min before being mounted on slides and coverslipped with Prolong Gold with DAPI (Thermo). Sections were then visualized using a confocal microscope.

For immunohistochemistry with DAB, a 10 min incubation in 0.3% hydrogen peroxide in PBS and 3 x 5 min PBS washes preceded the blocking/permeabilization step. A biotinylated secondary antibody was used, followed by a 1 hr incubation in ABC (Vector Labs). DAB (Vector Labs) was then used to deposit the stain at the site of antigen. Sections were then visualized using a brightfield microscope.

***In situ* hybridization (ISH) with RNA scope—**Cryostat sections (14 μm) for FISH experiments were made from PFA perfusion-fixed and 30% sucrose cryopreserved brains that were embedded in OCT freezing media. On-slide labeling was performed using

Author Manuscript Author Manuscript Author Manuscript Author Manuscript

RNAscope ISH technology and its associated kits. Probes against *Vat1l, Lypd1,* and *Nefh* (ACD Biotech, #495401, #318361, #443671) were used to label L5b cells in Colgalt2 and Gprin3 sections using the RNAscope Multiplex Fluorescent Reagent Kit v2 (ACD Biotech, #323100). All steps were carried out according to manufacturer recommendations in protocol #323100-USM, available on the manufacturer website.

Immunostaining after ISH was performed on-slide as described above, and concentrations for serums, Triton, and antibodies, as well as incubation times, were identical to free-floating immunostaining protocol.

Microscopic imaging—A Zeiss Axio Observer.Z1 with LSM 700 confocal microscope equipped with 50 mW, 400–640 nm lasers were used for all fluorescent visualizations. Zen software (Zeiss) was used for acquisition of images. FIJI (ImageJ, SciJava) was used for brightness and contrast adjustments, as well as image analysis (Rueden et al., 2017; Schindelin et al., 2012; Schneider et al., 2012). Tiled, brightfield images of whole DAB-stained sections were acquired using a Zeiss Axio Imager.M2 and Neurolucida (Micro Bright Field).

Multi-channel signal co-localization—For co-localization analyses, position markers were placed in FIJI over any cells that stained positive for a given marker. The position markers were saved as ROIs and placed over the next channel image of interest. The number of points that were positive in this second channel was counted as being double-positive. This analysis framework was used for CTB/GFP retrograde tracing analyses, and for L5b marker co-localization analyses in RNAscope experiments.

Soma size and cell count measurements—Soma sizes were determined in FIJI by tracing an ROI around EGFP+ cell soma (including the most proximal in-plane component of the apical dendrite) and measuring the area of the ROI in μm^2.

For determining loss of EGFP+ cells in SOD1*G93A mice, a 3 x 2 x 3 (w x h x z) z-stack tile scan of 20X fields was acquired on the confocal microscope. Every 6th section between +1.00 mm and +0.00 mm to Bregma was imaged (one section every ~240 μm), with each hemisphere being imaged separately. The z-stacks were collapsed in FIJI using the maximum intensity projection. Cells were then counted only if apical dendrite was clearly visible. All counting was performed blind to disease condition. Data are presented as percent of WT mean at each Bregma coordinate along the AP extent of M1.

Cell depth analyses—Cell depths were determined using a custom script (https://doi.org/10.5281/zenodo.6320615) written for FIJI/ImageJ that calculates the percentage depth from pia and white matter. The pial and white matter surfaces were manually delineated, and the points were placed on the image to mark the locations of the cells. The algorithm then drew a reference line perpendicular to the pial line that intersected the cell's point and terminated at the intersection with the white matter line. The cell's percent distance from the pial line along the reference line was then calculated and reported as a percentage depth from pia.

Author Manuscript Author Manuscript Author Manuscript Author Manuscript

Mitochondrial morphology analyses—Images of fluorescently-labeled mitochondria following MitoGFP or mCherry-TOM20 viral expression and immunostaining were collected at 63X-100X magnification and analyzed in FIJI/ImageJ. Cytoplasmic space (excluding the nucleus) was outlined for each neuronal cell body for which an apical dendrite could be observed. Data within the cytoplasmic region was Top-Hat filtered using a radius of 5 pixels, and thresholded using the Iso_data function. Mitochondrial morphology was analyzed using MiNA (Valente et al., 2017) with high contrast = 400 and low contrast = 100. The "Particle Analyzer" tool was also used to quantify size, total area, number, and density of discrete "particles" of MitoGFP, COX6C, CYTC, and mCherry-TOMM20 signals.

TRAP sample processing—TRAP experiments from cortical cell types were performed as previously described (Heiman et al., 2014; Nectow et al., 2017), with minor adaptations. For cell type characterizations, ~P40 animals were sacrificed, and M1 cortex sub-dissected in ice-chilled HBSS containing 2.5 mM HEPES-KOH (pH 7.4), 35 mM glucose, 4 mM NaHCO3, and 100 μg/mL cycloheximide. Cortices from 3 animals were pooled per biological replicate, with 3 replicates per cell type being prepared in total (9 animals). Samples were homogenized in extraction buffer containing 10 mM HEPES-KOH (pH 7.4), 150 mM KCl, 5 mM MgCl2, 0.5 mM DTT, 100 μg/mL cycloheximide, RNasin (Promega) and SUPERase-In (Life Technologies) RNase inhibitors, and Complete-EDTA-free protease inhibitors (Roche), and then centrifuged at 2000 x g to clear lysate debris. IGEPAL CA-630 (NP-40, Sigma) and DHPC (Avanti Polar Lipids, Alabaster, AL) were added to the resulting supernatant to a concentration of 1% each, followed by 20,000 x g centrifugation. Polysomes were immunoprecipitated (IP'ed) using 100 μg custom monoclonal anti-GFP antibodies (50 μg of clone 19C8 with 50 μg of clone 19F7) bound to biotinylated Protein L (Pierce, Thermo Fisher) coated streptavidin-coated magnetic beads (Thermo Fisher), and washed with high salt buffer containing 10 mM HEPES-KOH (pH 7.4), 350 mM KCl, 5 mM MgCl2, 1% IGEPAL CA-630, 0.5 mM DTT, 100 μg/mL cycloheximide, and RNasin RNase inhibitors (Promega). Overnight IP's were eluted and purified using Absolutely RNA Nanoprep kit (Agilent). For disease TRAP cohorts, whole cortex (Colgalt2 samples) or M1 cortex (M1 input and Gprin3 samples) from the ~P110 (symptomatic) timepoint were collected from SOD1*G93A-crossed Colgalt2- and Gprin3-bacTRAP animals and healthy littermates, with each individual used as a separate replicate. Cortices were then homogenized, and polysomes were IP'ed as described above. RNA quality was assessed using Nanodrop spectrophotometer and Agilent 2100 Bioanalyzer. Samples with RNA integrity values >7 were used to prepare libraries for sequencing. Total RNA from TRAP IPs and whole tissue inputs (15 ng per sample) were amplified and converted to cDNA using the Nugen Ovation RNA-Seq System V2 kit. cDNAs were then fragmented to an average size of 250 b.p. using a Covaris C2 sonicator and libraries were made using the Illumina TrueSeq RNA Sample Preparation kit v2, following manufacturer's instructions. Libraries were sequenced at The Rockefeller University Genomics Resource Center using the Illumina NextSeq 500 platform to obtain 75 b.p. paired-end reads. Sequencing for the Colgalt2 ALS cohort was performed at the New York Genome Center on an Illumina HiSeq 2500 platform to generate 50 b.p. paired-end reads.

Author Manuscript Author Manuscript Author Manuscript Author Manuscript

Sequencing analyses—Sequence and transcript coordinates for mouse mm10 UCSC genome and gene models were retrieved from the Bioconductor Bsgenome.Mmusculus.UCSC.mm10 (version 1.4.0) and TxDb.Mmusculus.UCSC.mm10.knownGene (version 3.4.0) Bioconductor libraries respectively. RNA-seq reads are aligned to the genome using the subjunc method (version 1.30.6) in Rsubread (Liao et al., 2013) and exported as bigWigs normalized to reads per million using the rtracklayer package (version 1.40.6). Counts in genes were generated using featureCounts within the Rsubread package (version 1.30.6) with default settings and the TxDb.Mmusculus.UCSC.mm10.knownGene gene models. The number of raw reads, the percentage of uniquely mapped reads, and the percent of bases mapped to mRNA (coding + UTRs) for each sample is presented in Table S1. Differential expression analysis on whole gene counts was performed using all default parameters in DESeq2 (version 1.26.0 (Love et al., 2014); in RStudio (version 1.2.5033; https://www.rstudio.com/), with R (version 3.6.3; https://www.r-project.org). Gene ontology enrichment analyses were performed using Metascape (Zhou et al., 2019) with default parameters, with genes with mean counts per million >100 being used for these analyses. GO categories used for functional category expression analyses included GO:1990542 mitochondrial transmembrane transport, GO:0006979 response to oxidative stress, GO:0016209 antioxidant activity, GO:0006119 oxidative phosphorylation, and GO:0006099 tricarboxylic cycle.

QUANTIFICATION AND STATISTICAL ANALYSIS

Image analyses—Statistically significant differences in soma size were determined using one-way ANOVA with subsequent Tukey's multiple comparison test and an alpha value of 0.05. Differences in EGFP+ cell number across WT and SOD littermates were statistically assessed using unpaired t-tests with Holm-Sidak correction for multiple comparisons.

RNA-seq analyses—Statistical significance in differential expression analyses were performed using default parameters and tests in DESeq2 (Love et al., 2014).

Differences in expression level of genes belonging to functional groups/categories were statistically assessed by one-way ANOVA with subsequent Tukey multiple comparisons test, and alpha value of 0.05.

Supplementary Material

Refer to Web version on PubMed Central for supplementary material.

ACKNOWLEDGMENTS

This work was supported by NIH/NINDS grants R01NS091722 (E.F.S.) and R21NS105047 (E.F.S.), ALS Therapy Alliance Grant 2013-F-052 (E.F.S.), ALS Association grants 14DUYT and 1114-471-454 (E.F.S.), and a National Science Foundation Graduate Research Fellowship 2014165948 (M.V.M.). N.H. is an investigator of the Howard Hughes Medical Institute (HHMI). We thank The Rockefeller University Genomics Resource Center, Transgenic Services Laboratory, and Comparative Bioscience Center as well as the New York Genome Center for technical support. We also thank Dr. Thomas Carroll and Hasnahana Chetia for bioinformatics support, as well as Drs. Hemali Phatnani and Ines Ibanez-Tallon for critical discussions.

Author Manuscript Author Manuscript Author Manuscript Author Manuscript

REFERENCES

Adam-Vizi V, and Chinopoulos C (2006). Bioenergetics and the formation of mitochondrial reactive oxygen species. Trends Pharmacol. Sci 27, 639–645. [PubMed: 17056127]

Arlotta P, Molyneaux BJ, Chen J, Inoue J, Kominami R, and Macklis JD (2005). Neuronal subtype-specific genes that control corticospinal motor neuron development in vivo. Neuron 45, 207–221. [PubMed: 15664173]

Bareyre FM, Kerschensteiner M, Misgeld T,and Sanes JR (2005). Transgenic labeling of the corticospinal tract for monitoring axonal responses to spinal cord injury. Nat. Med 11, 1355–1360. [PubMed: 16286922]

Bergemalm D, Jonsson PA, Graffmo KS, Andersen PM, Brannstrom T, Rehnmark A, and Marklund SL (2006). Overloading of stable and exclusion of unstable human superoxide dismutase-1 variants in mitochondria of murine amyotrophic lateral sclerosis models. J. Neurosci 26, 4147–4154. [PubMed: 16624935]

Bowling AC, Schulz JB, Brown RH Jr., and Beal MF (1993). Superoxide dismutase activity, oxidative damage, and mitochondrial energy metabolism in familial and sporadic amyotrophic lateral sclerosis. J. Neurochem 61, 2322–2325. [PubMed: 8245985]

Boyd PJ, Tu WY, Shorrock HK, Groen EJN, Carter RN, Powis RA, Thomson SR, Thomson D, Graham LC, Motyl AAL, et al. (2017). Bioenergetic status modulates motor neuron vulnerability and pathogenesis in a zebrafish model of spinal muscular atrophy. PLoS Genet. 13, e1006744. [PubMed: 28426667]

Braak H, Brettschneider J, Ludolph AC, Lee VM, Trojanowski JQ, and Tredici KD (2013). Amyotrophic lateral sclerosis—a model of corticofugal axonal spread. Nat. Rev. Neurol 9, 708–714. [PubMed: 24217521]

Browne SE, Yang L, DiMauro JP, Fuller SW, Licata SC, and Beal MF (2006). Bioenergetic abnormalities in discrete cerebral motor pathways presage spinal cord pathology in the G93A SOD1 mouse model of ALS. Neurobiol. Dis 22, 599–610. [PubMed: 16616851]

Caviness VS Jr. (1975). Architectonic map of neocortex of the normal mouse. J. Comp. Neurol 164, 247–263. [PubMed: 1184785]

Cederquist GY, Azim E, Shnider SJ, Padmanabhan H, and Macklis JD (2013). Lmo4 establishes rostral motor cortex projection neuron subtype diversity. J. Neurosci 33, 6321–6332. [PubMed: 23575831]

Chiu AY, Zhai P, Dal Canto MC, Peters TM, Kwon YW, Prattis SM, and Gurney ME (1995). Age-dependent penetrance of disease in a transgenic mouse model of familial amyotrophic lateral sclerosis. Mol. Cell Neurosci 6, 349–362. [PubMed: 8846004]

Cook C, and Petrucelli L (2019). Genetic convergence brings clarity to the enigmatic red line in ALS. Neuron 101, 1057–1069. [PubMed: 30897357]

Cozzolino M, and Carri MT (2012). Mitochondrial dysfunction in ALS. Prog. Neurobiol 97, 54–66. [PubMed: 21827820]

DeJesus-Hernandez M, Mackenzie IR, Boeve BF, Boxer AL, Baker M, Rutherford NJ, Nicholson AM, Finch NA, Flynn H, Adamson J, et al. (2011). Expanded GGGGCC hexanucleotide repeat in noncoding region of C9ORF72 causes chromosome 9p-linked FTD and ALS. Neuron 72, 245–256. [PubMed: 21944778]

Doyle JP, Dougherty JD, Heiman M, Schmidt EF, Stevens TR, Ma G, Bupp S, Shrestha P, Shah RD, Doughty ML, et al. (2008). Application of a translational profiling approach for the comparative analysis of CNS cell types. Cell 135, 749–762. [PubMed: 19013282]

Economo MN, Clack NG, Lavis LD, Gerfen CR, Svoboda K, Myers EW, and Chandrashekar J (2016). A platform for brain-wide imaging and reconstruction of individual neurons. eLife 5, e10566. [PubMed: 26796534]

Economo MN, Viswanathan S, Tasic B, Bas E, Winnubst J, Menon V, Graybuck LT, Nguyen TN, Smith KA, Yao Z, et al. (2018). Distinct descending motor cortex pathways and their roles in movement. Nature 563, 79–84. [PubMed: 30382200]

Eisen A, Entezari-Taher M, and Stewart H (1996). Cortical projections to spinal motoneurons: changes with aging and amyotrophic lateral sclerosis. Neurology 46, 1396–1404. [PubMed: 8628489]

Author Manuscript Author Manuscript Author Manuscript Author Manuscript

Evans CS, and Holzbaur ELF (2019). Autophagy and mitophagy in ALS. Neurobiol. Dis 122, 35–40. [PubMed: 29981842]

Feng G, Mellor RH, Bernstein M, Keller-Peck C, Nguyen QT, Wallace M, Nerbonne JM, Lichtman JW, and Sanes JR (2000). Imaging neuronal subsets in transgenic mice expressing multiple spectral variants of GFP. Neuron 28, 41–51. [PubMed: 11086982]

Fogarty MJ, Noakes PG, and Bellingham MC (2015). Motor cortex layer V pyramidal neurons exhibit dendritic regression, spine loss, and increased synaptic excitation in the presymptomatic hSOD1(G93A) mouse model of amyotrophic lateral sclerosis. J. Neurosci 35, 643–647. [PubMed: 25589758]

Genc B, Jara JH, Lagrimas AK, Pytel P, Roos RP, Mesulam MM, Geula C, Bigio EH, and Ozdinler PH (2017). Apical dendrite degeneration, a novel cellular pathology for Betz cells in ALS. Sci. Rep 7, 41765. [PubMed: 28165465]

Gerfen CR, Economo MN, and Chandrashekar J (2018). Long distance projections of cortical pyramidal neurons. J. Neurosci. Res. 96, 1467–1475. [PubMed: 27862192]

Gong S, Zheng C, Doughty ML, Losos K, Didkovsky N, Schambra UB, Nowak NJ, Joyner A, Leblanc G, Hatten ME, et al. (2003). A gene expression atlas of the central nervous system based on bacterial artificial chromosomes. Nature 425, 917–925. [PubMed: 14586460]

Green DR, Galluzzi L, and Kroemer G (2011). Mitochondria and the autophagy-inflammation-cell death axis in organismal aging. Science 333, 1109–1112. [PubMed: 21868666]

Groh A, Meyer HS, Schmidt EF, Heintz N, Sakmann B, and Krieger P (2010). Cell-type specific properties of pyramidal neurons in neocortex underlying a layout that is modifiable depending on the cortical area. Cereb. Cortex 20, 826–836. [PubMed: 19643810]

Gu Z, Kalambogias J, Yoshioka S, Han W, Li Z, Kawasawa YI, Pochareddy S, Li Z, Liu F, Xu X, et al. (2017). Control of species-dependent cortico-motoneuronal connections underlying manual dexterity. Science 357, 400–404. [PubMed: 28751609]

Guo J-Z, Graves AR, Guo WW, Zheng J, Lee A, Rodríguez-González J, Li N, Macklin JJ, Phillips JW, Mensh BD, et al. (2015). Cortex commands the performance of skilled movement. eLife 4, e10774. [PubMed: 26633811]

Gurney ME, Pu H, Chiu AY, Dal Canto MC, Polchow CY, Alexander DD, Caliendo J, Hentati A, Kwon YW, Deng HX, et al. (1994). Motor neuron degeneration in mice that express a human Cu,Zn superoxide dismutase mutation. Science 264, 1772–1775. [PubMed: 8209258]

Hamanaka RB, and Chandel NS (2009). Mitochondrial reactive oxygen species regulate hypoxic signaling. Curr. Opin. Cell Biol 21, 894–899. [PubMed: 19781926]

Hammer RP Jr., Tomiyasu U, and Scheibel AB (1979). Degeneration of the human Betz cell due to amyotrophic lateral sclerosis. Exp. Neurol 63, 336–346. [PubMed: 437007]

Heiman M, Kulicke R, Fenster RJ, Greengard P, and Heintz N (2014). Cell type-specific mRNA purification by translating ribosome affinity purification (TRAP). Nat. Protoc 9, 1282–1291. [PubMed: 24810037]

Heiman M, Schaefer A, Gong S, Peterson JD, Day M, Ramsey KE, Suarez-Farinas M, Schwarz C, Stephan DA, Surmeier DJ, et al. (2008). A translational profiling approach for the molecular characterization of CNS cell types. Cell 135, 738–748. [PubMed: 19013281]

Hirst J, King MS, and Pryde KR (2008). The production of reactive oxygen species by complex I. Biochem. Soc. Trans 36, 976–980. [PubMed: 18793173]

Hooks BM, Mao T, Gutnisky DA, Yamawaki N, Svoboda K, and Shepherd GM (2013). Organization of cortical and thalamic input to pyramidal neurons in mouse motor cortex. J. Neurosci 33, 748–760. [PubMed: 23303952]

Hyder F, Rothman DL, and Bennett MR (2013). Cortical energy demands of signaling and nonsignaling components in brain are conserved across mammalian species and activity levels. Proc. Natl. Acad. Sci. U S A 110, 3549–3554. [PubMed: 23319606]

Irvin CW, Kim RB, and Mitchell CS (2015). Seeking homeostasis: temporal trends in respiration, oxidation, and calcium in SOD1 G93A Amyotrophic Lateral Sclerosis mice. Front. Cell Neurosci 9, 248. [PubMed: 26190973]

Jaarsma D, Haasdijk ED, Grashorn JA, Hawkins R, van Duijn W, Verspaget HW, London J, and Holstege JC (2000). Human Cu/Zn superoxide dismutase (SOD1) overexpression in mice

Author Manuscript Author Manuscript Author Manuscript Author Manuscript

causes mitochondrial vacuolization, axonal degeneration, and premature motoneuron death and accelerates motoneuron disease in mice expressing a familial amyotrophic lateral sclerosis mutant SOD1. Neurobiol. Dis 7, 623–643. [PubMed: 11114261]

Jaiswal MK (2014). Selective vulnerability of motoneuron and perturbed mitochondrial calcium homeostasis in amyotrophic lateral sclerosis: implications for motoneurons specific calcium dysregulation. Mol. Cell Ther 2, 26. [PubMed: 26056593]

Kawai R, Markman T, Poddar R, Ko R, Fantana AL, Dhawale AK, Kampff AR, and Olveczky BP (2015). Motor cortex is required for learning but not for executing a motor skill. Neuron 86, 800–812. [PubMed: 25892304]

Kawamata H, and Manfredi G (2010). Mitochondrial dysfunction and intracellular calcium dysregulation in ALS. Mech. Ageing Dev 131, 517–526. [PubMed: 20493207]

Kim J, Hughes EG, Shetty AS, Arlotta P, Goff LA, Bergles DE, and Brown SP (2017). Changes in the excitability of neocortical neurons in a mouse model of amyotrophic lateral sclerosis are not specific to corticospinal neurons and are modulated by advancing disease. J. Neurosci 37, 9037–9053. [PubMed: 28821643]

Kobayashi M, Li L, Iwamoto N, Nakajima-Takagi Y, Kaneko H, Nakayama Y, Eguchi M, Wada Y, Kumagai Y, and Yamamoto M (2009). The antioxidant defense system Keap1-Nrf2 comprises a multiple sensing mechanism for responding to a wide range of chemical compounds. Mol. Cell Biol 29, 493–502. [PubMed: 19001094]

Kohara N, Kaji R, Kojima Y, Mills KR, Fujii H, Hamano T, Kimura J, Takamatsu N, and Uchiyama T (1996). Abnormal excitability of the corticospinal pathway in patients with amyotrophic lateral sclerosis: a single motor unit study using transcranial magnetic stimulation. Electroencephalogr. Clin. Neurophysiol 101, 32–41. [PubMed: 8625875]

Kudin AP, Bimpong-Buta NY, Vielhaber S, Elger CE, and Kunz WS (2004). Characterization of superoxide-producing sites in isolated brain mitochondria. J. Biol. Chem 279, 4127–4135. [PubMed: 14625276]

Kwiatkowski TJ Jr., Bosco DA, Leclerc AL, Tamrazian E, Vanderburg CR, Russ C, Davis A, Gilchrist J, Kasarskis EJ, Munsat T, et al. (2009). Mutations in the FUS/TLS gene on chromosome 16 cause familial amyotrophic lateral sclerosis. Science 323, 1205–1208. [PubMed: 19251627]

Lawrence M, Gentleman R, and Carey V (2009). rtracklayer: an R package for interfacing with genome browsers. Bioinformatics 25, 1841–1842. [PubMed: 19468054]

Le Masson G, Przedborski S, and Abbott LF (2014). A computational model of motor neuron degeneration. Neuron 83, 975–988. [PubMed: 25088365]

Lee JM, Calkins MJ, Chan K, Kan YW, and Johnson JA (2003a). Identification of the NF-E2-related factor-2-dependent genes conferring protection against oxidative stress in primary cortical astrocytes using oligonucleotide microarray analysis. J. Biol. Chem 278, 12029–12038. [PubMed: 12556532]

Lee JM, Shih AY, Murphy TH, and Johnson JA (2003b). NF-E2-related factor-2 mediates neuroprotection against mitochondrial complex I inhibitors and increased concentrations of intracellular calcium in primary cortical neurons. J. Biol. Chem 278, 37948–37956. [PubMed: 12842875]

Lein ES, Hawrylycz MJ, Ao N, Ayres M, Bensinger A, Bernard A, Boe AF, Boguski MS, Brockway KS, Byrnes EJ, et al. (2007). Genome-wide atlas of gene expression in the adult mouse brain. Nature 445, 168–176. [PubMed: 17151600]

Lenaz G, Bovina C, D'Aurelio M, Fato R, Formiggini G, Genova ML, Giuliano G, Merlo Pich M, Paolucci U, Parenti Castelli G, et al. (2002). Role of mitochondria in oxidative stress and aging. Ann. N. Y. Acad. Sci 959, 199–213. [PubMed: 11976197]

Liao Y, Smyth GK, and Shi W (2013). The Subread aligner: fast, accurate and scalable read mapping by seed-and-vote. Nucleic Acids Res. 41, e108. [PubMed: 23558742]

Love MI, Huber W, and Anders S (2014). Moderated estimation of fold change and dispersion for RNA-seq data with DESeq2. Genome Biol. 15, 550. [PubMed: 25516281]

Mattiazzi M, D'Aurelio M, Gajewski CD, Martushova K, Kiaei M, Beal MF, and Manfredi G (2002). Mutated human SOD1 causes dysfunction of oxidative phosphorylation in mitochondria of transgenic mice. J. Biol. Chem 277, 29626–29633. [PubMed: 12050154]

Author Manuscript Author Manuscript Author Manuscript Author Manuscript

Moore AS, and Holzbaur EL (2016). Dynamic recruitment and activation of ALS-associated TBK1 with its target optineurin are required for efficient mitophagy. Proc. Natl. Acad. Sci. U S A 113, E3349–E3358. [PubMed: 27247382]

Muller FL, Liu Y, and Van Remmen H (2004). Complex III releases superoxide to both sides of the inner mitochondrial membrane. J. Biol. Chem. 279, 49064–49073. [PubMed: 15317809]

Nectow AR, Moya MV, Ekstrand MI, Mousa A, McGuire KL, Sferrazza CE, Field BC, Rabinowitz GS, Sawicka K, Liang Y, et al. (2017). Rapid molecular profiling of defined cell types using viral TRAP. Cell Rep. 19, 655–667. [PubMed: 28423326]

Nunnari J, and Suomalainen A (2012). Mitochondria: in sickness and in health. Cell 148, 1145–1159. [PubMed: 22424226]

Oswald MJ, Tantirigama ML, Sonntag I, Hughes SM, and Empson RM (2013). Diversity of layer 5 projection neurons in the mouse motor cortex. Front. Cell Neurosci 7, 174. [PubMed: 24137110]

Ozdinler PH, Benn S, Yamamoto TH, Guzel M, Brown RH Jr., and Macklis JD (2011). Corticospinal motor neurons and related subcerebral projection neurons undergo early and specific neurodegeneration in hSOD1G(3)A transgenic ALS mice. J. Neurosci 31, 4166–4177. [PubMed: 21411657]

Peixoto PM, Kim HJ, Sider B, Starkov A, Horvath TL, and Manfredi G (2013). UCP2 overexpression worsens mitochondrial dysfunction and accelerates disease progression in a mouse model of amyotrophic lateral sclerosis. Mol. Cell Neurosci 57, 104–110. [PubMed: 24141050]

Prudencio M, Belzil VV, Batra R, Ross CA, Gendron TF, Pregent LJ, Murray ME, Overstreet KK, Piazza-Johnston AE, Desaro P, et al. (2015). Distinct brain transcriptome profiles in C9orf72-associated and sporadic ALS. Nat. Neurosci 18, 1175–1182. [PubMed: 26192745]

Pun S, Santos AF, Saxena S, Xu L, and Caroni P (2006). Selective vulnerability and pruning of phasic motoneuron axons in motoneuron disease alleviated by CNTF. Nat. Neurosci 9, 408–419. [PubMed: 16474388]

Ragagnin AMG, Shadfar S, Vidal M, Jamali MS, and Atkin JD (2019). Motor neuron susceptibility in ALS/FTD. Front. Neurosci 13, 532. [PubMed: 31316328]

Ravits J, Paul P, and Jorg C (2007). Focality of upper and lower motor neuron degeneration at the clinical onset of ALS. Neurology 68, 1571–1575. [PubMed: 17485643]

Renton AE, Majounie E, Waite A, Simon-Sanchez J, Rollinson S, Gibbs JR, Schymick JC, Laaksovirta H, van Swieten JC, Myllykangas L, et al. (2011). A hexanucleotide repeat expansion in C9ORF72 is the cause of chromosome 9p21-linked ALS-FTD. Neuron 72, 257–268. [PubMed: 21944779]

Robberecht W, and Philips T (2013). The changing scene of amyotrophic lateral sclerosis. Nat. Rev. Neurosci 14, 248–264. [PubMed: 23463272]

Rosen DR, Siddique T, Patterson D, Figlewicz DA, Sapp P, Hentati A, Donaldson D, Goto J, O'Regan JP, Deng HX, et al. (1993). Mutations in Cu/Zn superoxide dismutase gene are associated with familial amyotrophic lateral sclerosis. Nature 362, 59–62. [PubMed: 8446170]

Rowland LP, and Shneider NA (2001). Amyotrophic lateral sclerosis. N. Engl. J. Med 344, 1688–1700. [PubMed: 11386269]

Rueden CT, Schindelin J, Hiner MC, DeZonia BE, Walter AE, Arena ET, and Eliceiri KW (2017). ImageJ2: ImageJ for the next generation of scientific image data. BMC Bioinformatics 18, 529. [PubMed: 29187165]

Saba L, Viscomi MT, Caioli S, Pignataro A, Bisicchia E, Pieri M, Molinari M, Ammassari-Teule M, and Zona C (2015). Altered functionality, morphology, and vesicular glutamate transporter expression of cortical motor neurons from a presymptomatic mouse model of amyotrophic lateral sclerosis. Cereb. Cortex 26, 1512–1528. [PubMed: 25596588]

Saberi S, Stauffer JE, Schulte DJ, and Ravits J (2015). Neuropathology of amyotrophic lateral sclerosis and its variants. Neurol. Clin 33, 855–876. [PubMed: 26515626]

Sasaki S, Warita H, Abe K, and Iwata M (2005). Impairment of axonal transport in the axon hillock and the initial segment of anterior horn neurons in transgenic mice with a G93A mutant SOD1 gene. Acta Neuropathol. 110, 48–56. [PubMed: 15920660]

Schindelin J, Arganda-Carreras I, Frise E, Kaynig V, Longair M, Pietzsch T, Preibisch S, Rueden C, Saalfeld S, Schmid B, et al. (2012). Fiji: an open-source platform for biological-image analysis. Nat. Methods 9, 676–682. [PubMed: 22743772]

Author Manuscript Author Manuscript Author Manuscript Author Manuscript

Schmidt EF, Warner-Schmidt JL, Otopalik BG, Pickett SB, Greengard P, and Heintz N (2012). Identification of the cortical neurons that mediate antidepressant responses. Cell 149, 1152–1163. [PubMed: 22632977]

Schneider CA, Rasband WS, and Eliceiri KW (2012). NIH image to ImageJ: 25 years of image analysis. Nat. Methods 9, 671–675. [PubMed: 22930834]

Scortegagna M, Ding K, Oktay Y, Gaur A, Thurmond F, Yan LJ, Marck BT, Matsumoto AM, Shelton JM, Richardson JA, et al. (2003). Multiple organ pathology, metabolic abnormalities and impaired homeostasis of reactive oxygen species in Epas1−/− mice. Nat. Genet 35, 331–340. [PubMed: 14608355]

Semenza GL (2001). HIF-1 and mechanisms of hypoxia sensing. Curr. Opin. Cell Biol 13, 167–171. [PubMed: 11248550]

Shoenfeld L, Westenbroek RE, Fisher E, Quinlan KA, Tysseling VM, Powers RK, Heckman CJ, and Binder MD (2014). Soma size and Cav1.3 channel expression in vulnerable and resistant motoneuron populations of the SOD1G93A mouse model of ALS. Physiol. Rep 2, e12113. [PubMed: 25107988]

Sreedharan J, Blair IP, Tripathi VB, Hu X, Vance C, Rogelj B, Ackerley S, Durnall JC, Williams KL, Buratti E, et al. (2008). TDP-43 mutations in familial and sporadic amyotrophic lateral sclerosis. Science 319, 1668–1672. [PubMed: 18309045]

Suter BA, Migliore M, and Shepherd GM (2013). Intrinsic electrophysiology of mouse corticospinal neurons: a class-specific triad of spike-related properties. Cereb. Cortex 23, 1965–1977. [PubMed: 22761308]

Tam OH, Rozhkov NV, Shaw R, Kim D, Hubbard I, Fennessey S, Propp N, Fagegaltier D, Harris BT, Ostrow LW, et al. (2019). Postmortem cortex samples identify distinct molecular subtypes of ALS: retrotransposon activation, oxidative stress, and activated glia. Cell Rep. 29, 1164–1177.e5. [PubMed: 31665631]

Tandan R, and Bradley WG (1985). Amyotrophic lateral sclerosis: part 1. Clinical features, pathology, and ethical issues in management. Ann. Neurol 18, 271–280. [PubMed: 4051456]

Tasic B, Menon V, Nguyen TN, Kim TK, Jarsky T, Yao Z, Levi B, Gray LT, Sorensen SA, Dolbeare T, et al. (2016). Adult mouse cortical cell taxonomy revealed by single cell transcriptomics. Nat. Neurosci 19, 335–346. [PubMed: 26727548]

Tasic B, Yao Z, Graybuck LT, Smith KA, Nguyen TN, Bertagnolli D, Goldy J, Garren E, Economo MN, Viswanathan S, et al. (2018). Shared and distinct transcriptomic cell types across neocortical areas. Nature 563, 72–78. [PubMed: 30382198]

Thomsen GM, Gowing G, Latter J, Chen M, Vit JP, Staggenborg K, Avalos P, Alkaslasi M, Ferraiuolo L, Likhite S, et al. (2014). Delayed disease onset and extended survival in the SOD1G93A rat model of amyotrophic lateral sclerosis after suppression of mutant SOD1 in the motor cortex. J. Neurosci 34, 15587–15600. [PubMed: 25411487]

Twig G, and Shirihai OS (2011). The interplay between mitochondrial dynamics and mitophagy. Antioxid. Redox Signal 14, 1939–1951. [PubMed: 21128700]

Valente AJ, Maddalena LA, Robb EL, Moradi F, and Stuart JA (2017). A simple ImageJ macro tool for analyzing mitochondrial network morphology in mammalian cell culture. Acta Histochem 119, 315–326. [PubMed: 28314612]

Vance C, Rogelj B, Hortobagyi T, De Vos KJ, Nishimura AL, Sreedharan J, Hu X, Smith B, Ruddy D, Wright P, et al. (2009). Mutations in FUS, an RNA processing protein, cause familial amyotrophic lateral sclerosis type 6. Science 323, 1208–1211. [PubMed: 19251628]

Vandoorne T, De Bock K, and Van Den Bosch L (2018). Energy metabolism in ALS: an underappreciated opportunity? Acta Neuropathol. 135, 489–509. [PubMed: 29549424]

Vucic S, Ziemann U, Eisen A, Hallett M, and Kiernan MC (2013). Transcranial magnetic stimulation and amyotrophic lateral sclerosis: pathophysiological insights. J. Neurol. Neurosurg. Psychiatry 84, 1161–1170. [PubMed: 23264687]

Wang X, and Michaelis EK (2010). Selective neuronal vulnerability to oxidative stress in the brain. Front. Aging Neurosci 2, 12. [PubMed: 20552050]

Author Manuscript Author Manuscript Author Manuscript Author Manuscript

Wang X, Zaidi A, Pal R, Garrett AS, Braceras R, Chen XW, Michaelis ML, and Michaelis EK (2009). Genomic and biochemical approaches in the discovery of mechanisms for selective neuronal vulnerability to oxidative stress. BMC Neurosci. 10, 12. [PubMed: 19228403]

Wong YC, and Holzbaur EL (2014). Optineurin is an autophagy receptor for damaged mitochondria in parkin-mediated mitophagy that is disrupted by an ALS-linked mutation. Proc. Natl. Acad. Sci. U S A 111, E4439–E4448. [PubMed: 25294927]

Yasvoina MV, Genc B, Jara JH, Sheets PL, Quinlan KA, Milosevic A, Shepherd GM, Heckman CJ, and Ozdinler PH (2013). eGFP expression under UCHL1 promoter genetically labels corticospinal motor neurons and a subpopulation of degeneration-resistant spinal motor neurons in an ALS mouse model. J. Neurosci 33, 7890–7904. [PubMed: 23637180]

Yu J, Anderson CT, Kiritani T, Sheets PL, Wokosin DL, Wood L, and Shepherd GM (2008). Local-circuit phenotypes of layer 5 neurons in motorfrontal cortex of YFP-H mice. Front. Neural Circuits 2, 6. [PubMed: 19129938]

Zanette G, Tamburin S, Manganotti P, Refatti N, Forgione A, and Rizzuto N (2002). Different mechanisms contribute to motor cortex hyperexcitability in amyotrophic lateral sclerosis. Clin. Neurophysiol 113, 1688–1697. [PubMed: 12417221]

Zang DW, and Cheema SS (2002). Degeneration of corticospinal and bulbospinal systems in the superoxide dismutase 1(G93A G1H) transgenic mouse model of familial amyotrophic lateral sclerosis. Neurosci. Lett 332, 99–102. [PubMed: 12384220]

Zhou Y, Zhou B, Pache L, Chang M, Khodabakhshi AH, Tanaseichuk O, Benner C, and Chanda SK (2019). Metascape provides a biologist-oriented resource for the analysis of systems-level datasets. Nat. Commun 10, 1523. [PubMed: 30944313]

Author Manuscript Author Manuscript Author Manuscript Author Manuscript

Highlights

- Gprin3 and Colgalt2 bacTRAP mice label distinct subtypes of layer 5b neurons in M1
- Gprin3 cells degenerate in a preclinical model of ALS, whereas Colgalt2 cells do not
- Regulation of bioenergetics-related genes is a common disease response of L5b cells
- Gprin3 genetic properties imply higher energy demand and oxidative stress sensitivity

Author Manuscript Author Manuscript Author Manuscript Author Manuscript

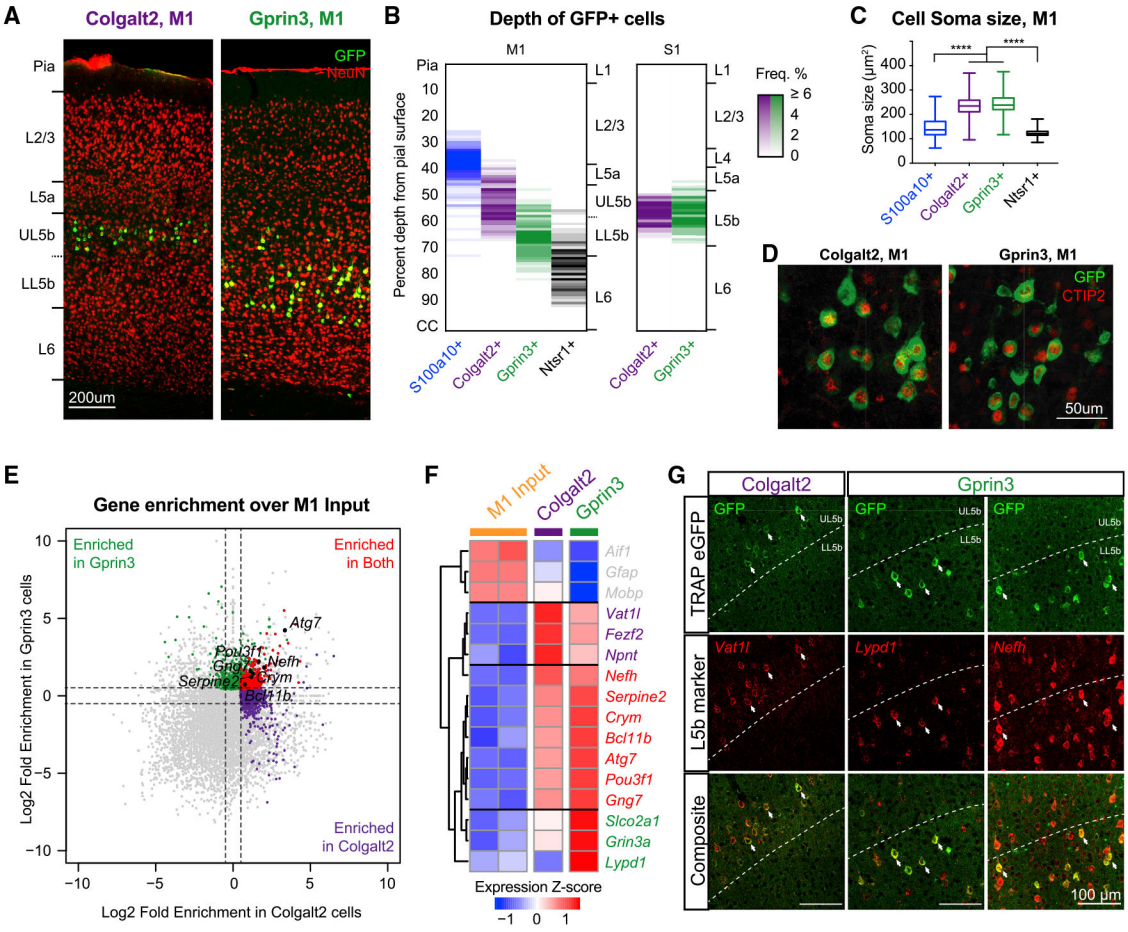

Figure 1. Colgalt2 and Gprin3 bacTRAP lines label molecularly and anatomically distinct populations of projection neurons in layer 5b of M1

(A) Anti-GFP immunostaining (green) showing expression of eGFP-L10a in deep-layer cells in M1 of Colgalt2-bacTRAP DU9 (left) and Gprin3-bacTRAP ES152 (right) animals. Red staining indicates NeuN + cells. Scale bar, 200 μm.

(B) Frequency distribution of laminar depth of labeled cells in Colgalt2-bacTRAP (purple, n = 209 cells), Gprin3-bacTRAP (green, n = 163 cells), S100a10-bacTRAP (blue, n = 248 cells), and Ntsr1-bacTRAP (black, n = 146 cells) mice in M1 and in neighboring S1 (L5b populations only, Colgalt2-bacTRAP, n = 125; Gprin3-bacTRAP, n = 95 cells).

(C) Box and whisker plots of population distribution for soma sizes (area in μm^2) of S100a10 (blue, mean ± SEM 144.2 ± 1.7 μm^2), Colgalt2 (purple, 233.3 ± 2.6 μm^2), Gprin3 (green, 244.0 ± 2.7 μm^2), and Ntsr1 (black, 122.3 ± 1.3 μm^2) cells. ****$p < 0.0001$ by one-way ANOVA and subsequent Tukey multiple comparison test.

(D) Immunostaining for CTIP2 (red) and GFP (green) in Colgalt2-bacTRAP (left) and Gprin3-bacTRAP (right) animals. Scale bar, 50 μm.

(E) Scatterplot showing Log_2 fold enrichment values from DE analyses of Colgalt2 TRAP vs. M1 input (x axis) and Gprin3 TRAP vs. M1 input (y axis). Genes enriched in Colgalt2 only (purple), Gprin3 only (green), or both (red) are indicated. L5b PT cell marker genes (black) are labeled.

Author Manuscript Author Manuscript Author Manuscript Author Manuscript

(F) Heatmap showing relative expression of glial genes (gray) and a subset of known L5b marker genes that showed enrichment in either Colgalt2 cells only (purple), both cell types (red), or Gprin3 cells only (green) across M1 input, Colgalt2 TRAP, and Gprin3 TRAP datasets. Values are reported as z-scores of normalized CPM, averaged across biological replicates, and scaled for each gene.

(G) Images showing FISH for *Vat1l* in UL5b (left column), *Lypd1* in LL5b (middle column), and *Nefh* in both sublayers (right column) co-labeled with anti-GFP immunofluorescence in M1 of bacTRAP mice. Arrows indicate cells that were double-positive for GFP and the probed marker gene. Scale bar, 100 μm. See also Figures S1 and S2 and Tables S1 and S2.

Author Manuscript Author Manuscript Author Manuscript Author Manuscript

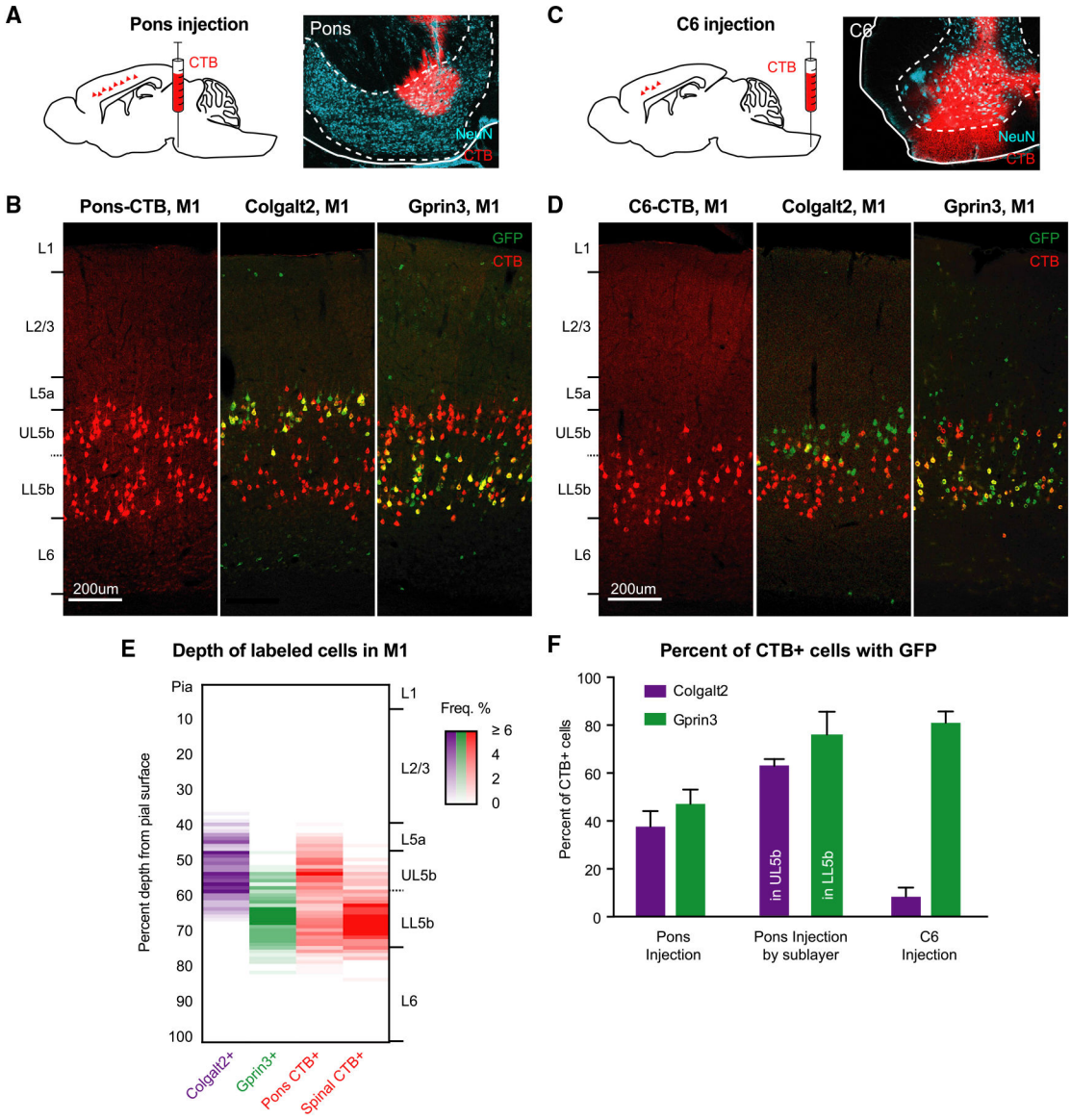

Figure 2. Retrograde tracing reveals overlapping and distinct axonal projection targets of Colgalt2 and Gprin3 cells

(A) Schematic illustration of the strategy for retrograde tracing of corticopontine neurons with cholera toxin B (CTB; left), and a representative image of the injection site (right) showing anti-CTB (red) and anti-NeuN (cyan) immunofluorescence.

(B) Immunofluorescent images showing anti-CTB-labeled cells (red) in both sublayers of L5b in M1 following an injection into the pons (right). Staining with anti-GFP (green) revealed overlap of labeled cells in UL5b of Colgalt2-bacTRAP animals (middle) and LL5b in Gprin3-bacTRAP (right) animals. Scale bar, 200 μm.

(C) Schematic of the strategy for retrograde labeling of corticospinal neurons (left) and a representative image of the injection site in C6 spinal cord (right) showing anti-CTB (red) and anti-NeuN (cyan) immunofluorescence.

Author Manuscript Author Manuscript Author Manuscript Author Manuscript

(D) Immunofluorescent images, as in (B), showing CTB- and GFP-labeled cells in LL5b of M1 (left) in Gprin3-bacTRAP (right) and Colgalt2-bacTRAP (center) mice following C6 injections. Scale bar, 200 μm.

(E) Histogram of the quantification of laminar depth of GFP+ Colgalt2 (purple, n = 209 cells) and Gprin3 (green, n = 163) cells alongside CTB+ corticopontine (red left, n = 651 cells) and corticospinal cells (red right, n = 192 cells). Frequency reported as percentage of total cells found at each depth.

(F) Quantification (mean ± SEM) of the percentage of M1 CTB+ cells that were GFP+ in Colgalt2-bacTRAP (purple) or Gprin3-bacTRAP (green) animals across all of L5b (left), or within each individual sublayer (middle) after pons injections. Right: the percentage (mean ± SEM) of double-labeled cells in M1 of each bacTRAP line following injections into C6. See also Figure S3.

Author Manuscript Author Manuscript Author Manuscript Author Manuscript

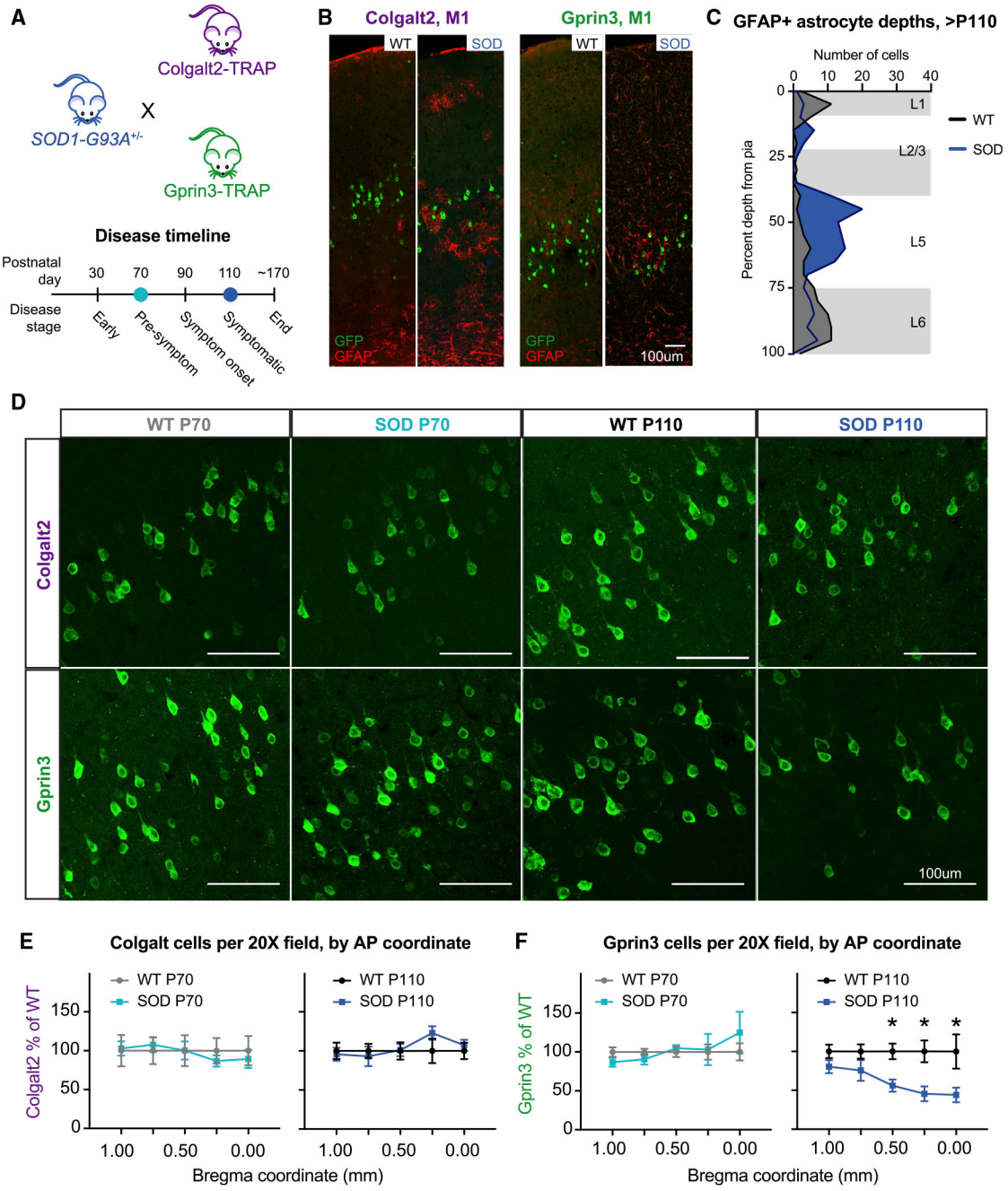

Figure 3. Loss of Gprin3 cells, but not Colgalt2 cells, in symptomatic SOD1-G93A mice

(A) Schematic of breeding paradigm for SOD1-G93A and bacTRAP animals (top) and the timeline of disease progression used for histology and sequencing (bottom).

(B) Immunofluorescent images of M1 from Colgalt2-bacTRAP and Gprin3-bacTRAP animals at the symptomatic time point, showing GFP (green) and the activated astrocyte marker, GFAP (red), across healthy (WT) or disease (SOD) conditions. Scale bar, 100 μm.

(C) Frequency distribution of laminar depth of GFAP+-activated astrocytes across healthy (WT, gray, n = 83 cells) and disease (SOD, blue, n = 130 cells) conditions at age >P110. Frequency is reported as absolute number of GFAP+ cells found at each depth.

Author Manuscript Author Manuscript Author Manuscript Author Manuscript

(D) Representative images showing GFP+ cells in M1 of Colgalt2-bacTRAP (top row) or Gprin3-bacTRAP (bottom row) mice at pre-symptomatic (P70) and symptomatic (P110) time points in WT and symptomatic SOD animals. Scale bars, 100 μm.
(E and F) Quantification (mean ± SEM) of the number of GFP+ cells along the rostrocaudal axis of M1 at pre-symptomatic (left) and symptomatic (right) time points in healthy (WT, grays) and disease (SOD, blues) conditions for (E) the Colgalt2 bacTRAP line (WT P70 n = 5 animals, SOD P70 n = 8 animals; Colgalt2 WT P110 n = 7 animals, SOD P110, n = 5), and (F) the Gprin3 bacTRAP line (Gprin3 WT P70 n = 8 animals, SOD P70 n = 5 animals; Gprin3 WT P110 n = 7 animals, SOD P110 n = 5 animals). *$p < 0.05$ by unpaired t test with Holm-Sidak correction for multiple comparisons. See also Figure S4.

Author Manuscript Author Manuscript Author Manuscript Author Manuscript

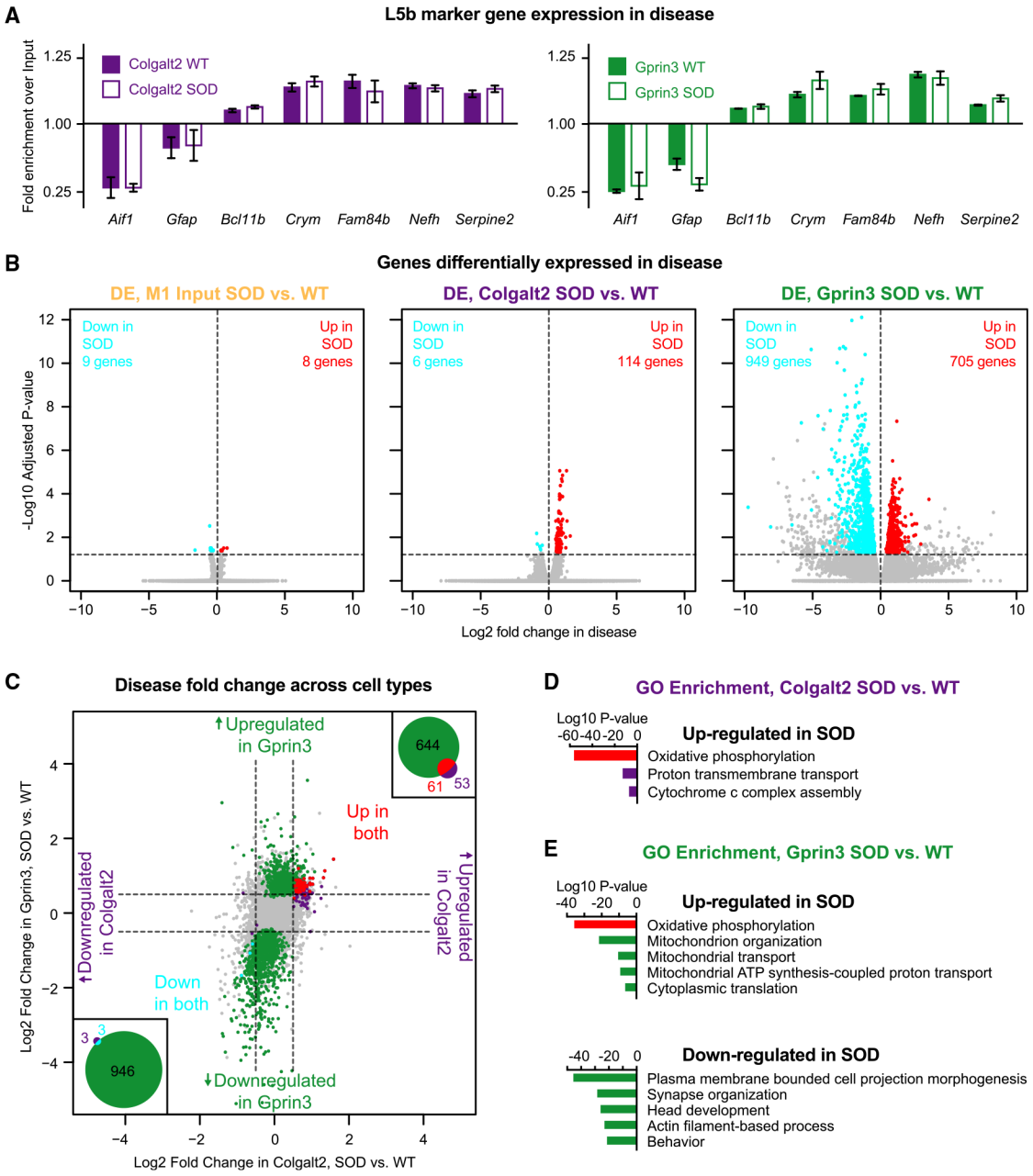

Figure 4. Gprin3 cells show a robust molecular response to SOD1-G93A expression

(A) Bar graphs showing relative expression (mean ± SD CPM) of glial and L5b marker genes across healthy (WT) and diseased (SOD) TRAP samples from Colgalt2 and Gprin3 cells compared with sample-matched M1 input.

(B) Volcano plots identifying DE genes between WT and SOD littermates for M1 input (left), Colgalt2 TRAP (middle), and Gprin3 TRAP (right) samples. Genes significantly up-regulated (red) or down-regulated (cyan) in SOD are indicated. Dotted lines represent significance thresholds of 0.0 $\log_2$ fold change (vertical line) and 1.3 $-\log_{10}$ padj (horizontal line).

Author Manuscript Author Manuscript Author Manuscript Author Manuscript

(C) Scatterplot comparing SOD-mediated $\log_2$ fold changes in Colgalt2 TRAP (x axis) and Gprin3 TRAP (y axis) samples for all genes that had mean CPM >100 in Gprin3 cells. Purple and green dots highlight genes that were significantly changed only in Colgalt2 cells or Gprin3 cells, respectively; genes that were changed in both cell types are highlighted in red (up-regulated) or cyan (down-regulated). Dotted lines represent $\log_2$ fold change of ±0.5. Insets show Venn diagrams indicating the total number of genes that were uniquely or commonly upregulated (top right) or downregulated (bottom left) across both cell types. (D) Summary of GO enrichment analysis of DE genes in Colgalt2 TRAP data from (B). (E) Summary of GO enrichment analysis of DE genes in Gprin3 TRAP data from (B). Red bars in (D) and (E) indicate a category that was common to both cell types. See also Figure S5 and Tables S1 and S3.

Author Manuscript Author Manuscript Author Manuscript Author Manuscript

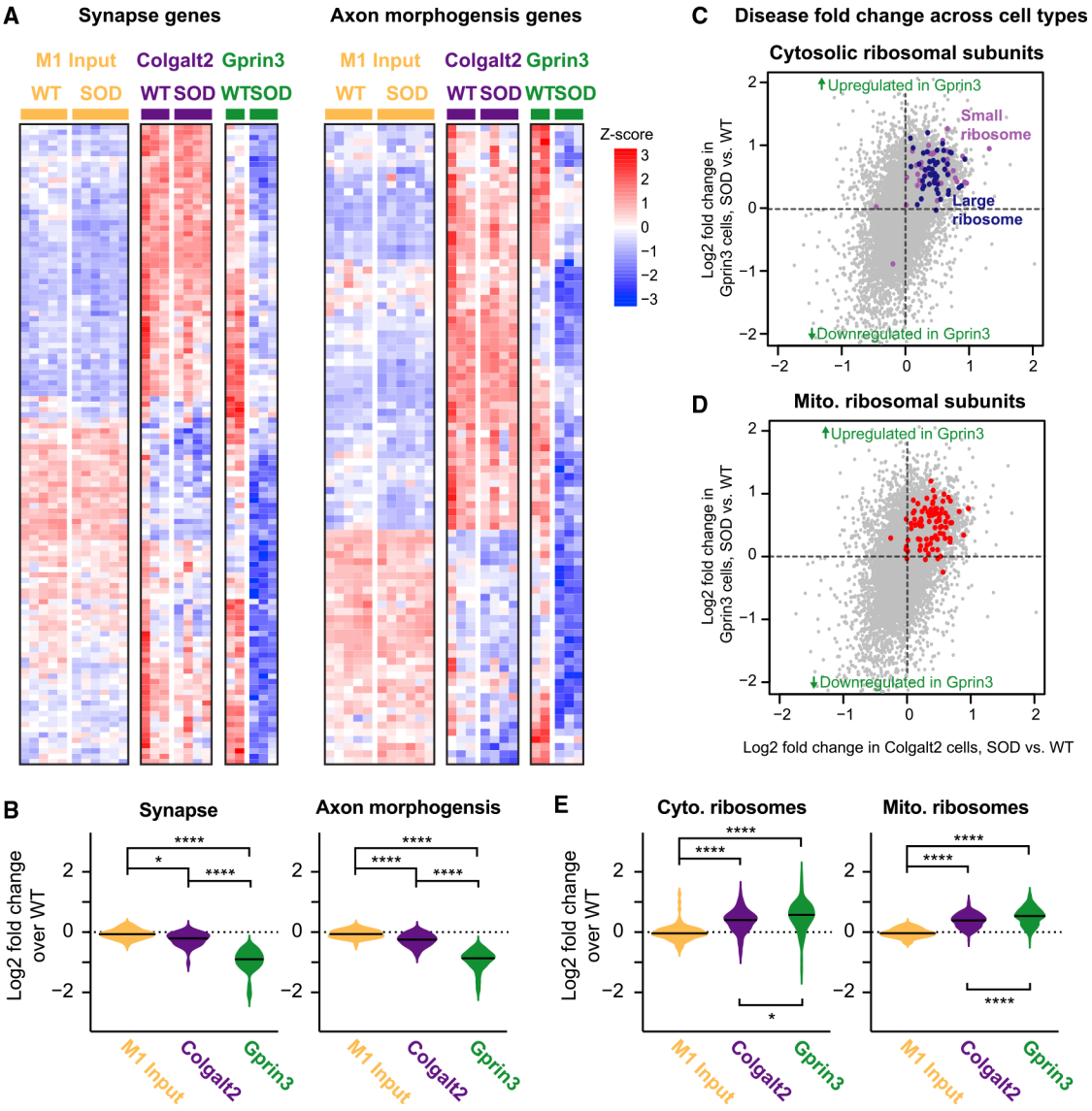

Figure 5. Gprin3 cells modulate ribosomal, axon morphogenesis, and synapse structure and function genes in disease

(A) Heatmaps showing relative expression of genes that encode synaptic (left) and axon morphogenesis (right) proteins in M1 input, Colgalt2 TRAP, and Gprin3 TRAP samples across WT and SOD replicates. Values are reported as z-scores for normalized CPM, scaled for each gene.

(B) Violin plots of SOD-mediated $\log_2$ fold change values for all synapse (left) and axonal (right) genes that showed a significant change in Gprin3 cells across M1 input, Colgalt2, and Gprin3 cells.

(C) Scatterplot showing SOD-mediated $\log_2$ fold changes in Colgalt2 (x axis) and Gprin3 (y axis) TRAP samples for cytosolic ribosomal subunit genes (top, blue and lilac dots) and mitochondrial ribosome genes (bottom, red dots) among all genes that had mean CPM >100 in Gprin3 cells.

(D) Violin plots of SOD-mediated $\log_2$ fold change values of cytoplasmic (left) and mitochondrial (right) ribosome genes from (C) across M1 input, Colgalt2 TRAP, and Gprin3 TRAP samples. For (B) and (D), *$p < 0.05$ and ****$p < 0.00001$ by one-way ANOVA and subsequent Tukey multiple comparison test. See also Figures S5 and S6.

Author Manuscript Author Manuscript Author Manuscript Author Manuscript

Author Manuscript Author Manuscript Author Manuscript Author Manuscript

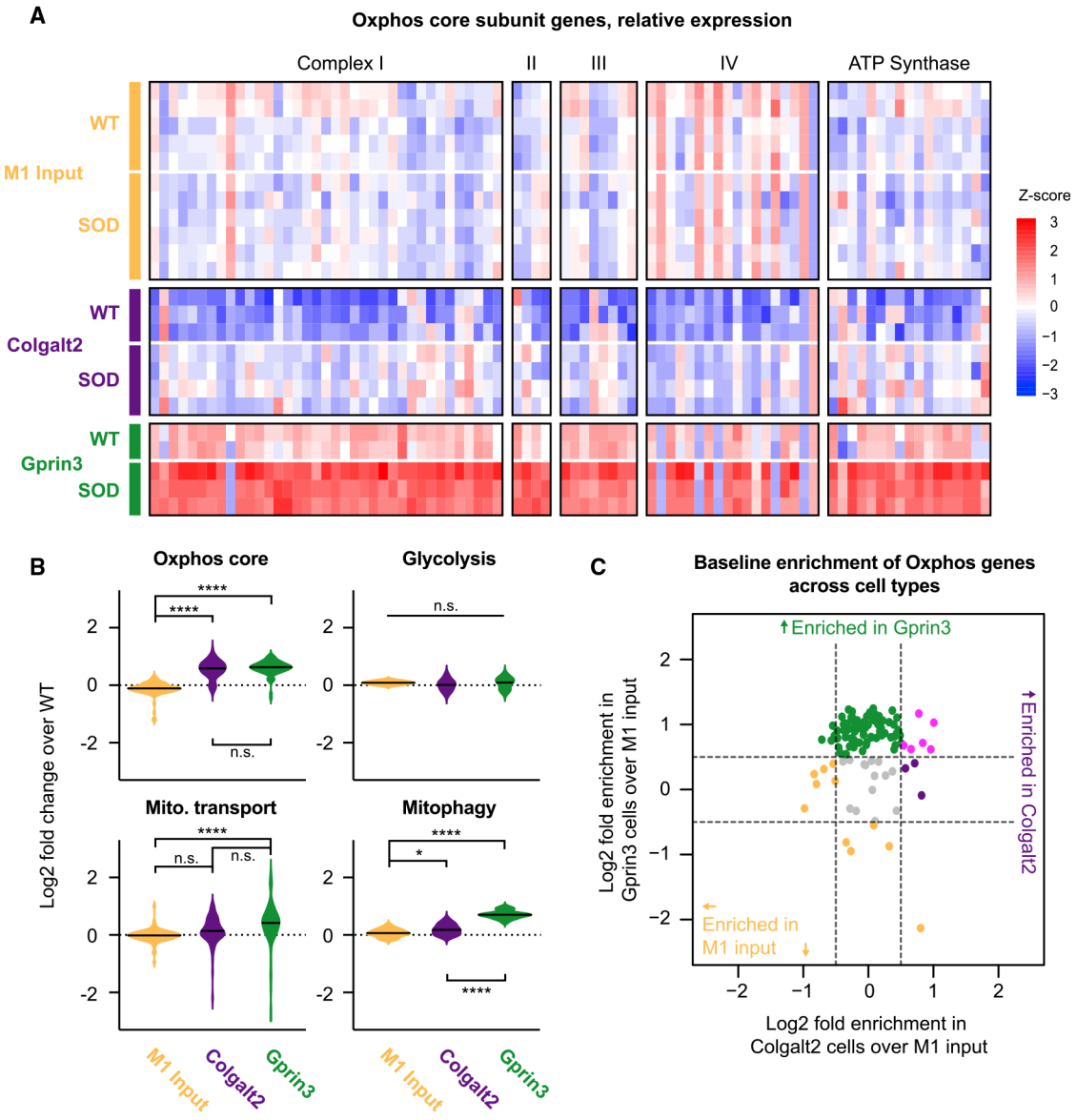

Figure 6. SOD1-G93A-mediated regulation of oxidative phosphorylation in layer 5b PT neurons

(A) Heatmap showing relative expression of genes encoding each subunit of the Oxphos complexes in each experimental condition. Values are reported as z-scores for normalized CPM, scaled for each gene.

(B) Violin plots of SOD-mediated $\log_2$ fold change values for all Oxphos core subunit and glycolysis genes (top), as well as all mitochondrial transmembrane transport and mitophagy genes (bottom) across M1 input, Colgalt2 TRAP, and Gprin3 TRAP samples. *$p < 0.05$, ****$p < 1 \times 10^{-7}$; n.s., not significant by one-way ANOVA and subsequent Tukey multiple comparison test.

(C) Scatterplot comparing the enrichment of Oxphos genes in Colgalt2 (x axis) and Gprin3 (y axis) at baseline. Genes enriched in Gprin3 only (green), Colgalt2 only (purple), both L5b cell types (magenta), or depleted from each cell type relative to M1 input (orange) are indicated. See also Figures S6 and S7.

Author Manuscript Author Manuscript Author Manuscript Author Manuscript

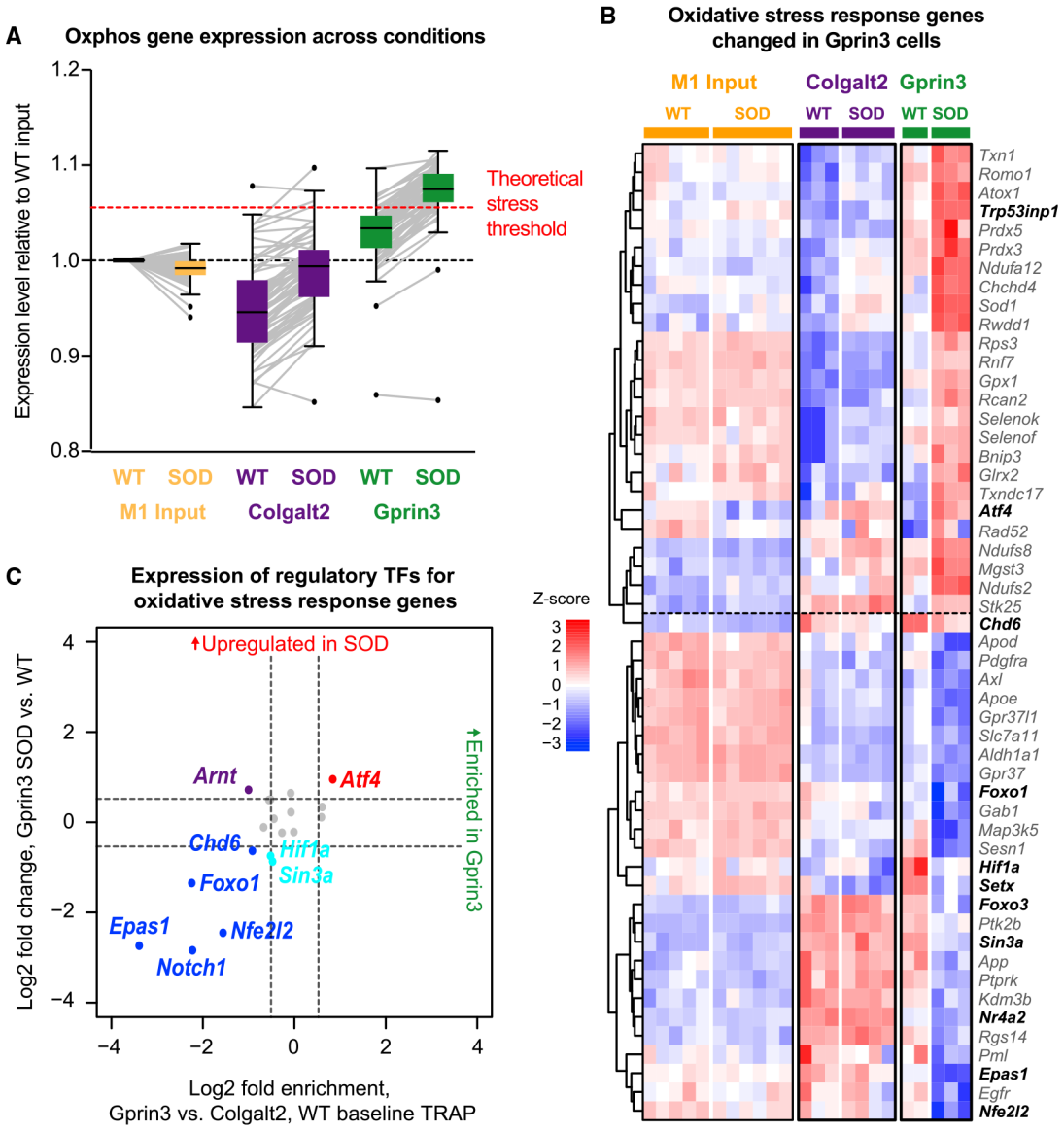

Figure 7. Oxidative stress response genes are modulated in Gprin3 cells, and hypoxia- and oxidative stress-responsive transcription factors are depleted in healthy Gprin3 cells

(A) Box and whisker plot showing ratio of CPMs of genes that comprise the Oxphos core subunits relative to WT M1 input for WT and SOD datasets across M1 input, Colgalt2 TRAP, and Gprin3 TRAP samples. Gray lines indicate trajectory of change for each individual Oxphos gene. Dotted red line highlights a theoretical threshold above which Oxphos gene expression levels may trigger oxidative stress pathways.

(B) Heatmap showing relative expression across all samples of genes involved in oxidative stress and antioxidant responses that were significantly changed in Gprin3 cell. Genes that code for transcription factors are in bolded text. Values are reported as z-scores for normalized CPM, scaled for each gene.

(C) Scatterplot comparing enrichment of genes encoding transcription factors associated with activation of hypoxia and oxidative stress response pathways between Gprin3 and.

Author Manuscript Author Manuscript Author Manuscript Author Manuscript

Colgalt2 at baseline (x axis) and Gprin3 cells in disease (y axis). Genes significantly depleted in Gprin3 compared with Colgalt2 and significantly down-regulated in disease (blue), down-regulated in disease but not enriched in either cell type (cyan), depleted in Gprin3 cells but not changed in disease (purple), and up-regulated in disease but not enriched in either cell type (red) are indicated. See also Figure S8.

Author Manuscript Author Manuscript Author Manuscript Author Manuscript

KEY RESOURCES TABLE

REAGENT or RESOURCE	SOURCE	IDENTIFIER
Antibodies		
Chicken polyclonal anti-GFP	Abcam	Cat# Ab13970; RRID: AB_300798
Mouse monoclonal anti-NeuN, clone A60	EMD Millipore	Cat# MAB377; RRID: AB_2298772
Rabbit polyclonal anti-GFAP	Thermo Fisher	Cat# RB-087-A0; RRID: AB_60417
Rabbit polyclonal anti-Cholera Toxin Beta	Abcam	Cat# Ab34992; RRID: AB_726859
Rabbit polyclonal anti-RFP	Abcam	Cat# Ab62341; RRID: AB_945213
Rabbit polyclonal anti-COX6C	Thermo Fisher	Cat# PA5-38900; RRID: AB_2555492
Mouse monoclonal anti-Cytochrome C	Abcam	Cat# Ab110325; RRID: AB_10864775
Donkey polyclonal anti-Rabbit, Cyanine 3-conjugated	Jackson Immunoresearch	Cat# 711-165-152; RRID: AB_2307443
Donkey polyclonal anti-Chicken, Alexa 488-conjugated	Jackson Immunoresearch	Cat# 703-545-155; RRID: AB_2340375
Donkey polyclonal anti-Mouse, Alexa 647-conjugated	Jackson Immunoresearch	Cat# 715-605-150; RRID: AB_2340862
Mouse monoclonal anti-GFP, clone Htz-GFP-19F7	Memorial Sloan-Kettering Monoclonal Antibody Facility	RRID: AB_2716736
Mouse monoclonal anti-GFP, clone Htz-GFP-19C8	Memorial Sloan-Kettering Monoclonal Antibody Facility	RRID: AB_2716737
Chemicals, peptides, and recombinant proteins		
Cholera Toxin Beta, Alexa 555-conjugated	Thermo Fisher	Cat# C34776
Vetbond	3M	Cat# 70200742529
Colorless Neg-50 Medium	VWR	Cat# 84000-154
Tissue-Tek O.C.T Compound	Sakura	Cat# 4583
Normal Donkey Serum	Jackson Immunoresearch	Cat# 017-000-121
Triton X-100	Millipore Sigma	Cat# X100-100ML; CAS: 9002-93-1
ProLong Gold Antifade Mounting Mountant with DAPI	Thermo Fisher	Cat# P36931
RNAscope Probe Mm-Vat1l	ACD Bio	Cat# 495401
RNAscope Probe Mm-Lypd1	ACD Bio	Cat# 318361
RNAscope Probe Mm-Nefh	ACD Bio	Cat# 443671
Bovine Serum Albumin, IgG and protease-free	Jackson Immunoresearch	Cat# 001-000-162
Cycloheximide	Millipore Sigma	Cat# C7698; CAS: 66-81-9
DL-DTT	Millipore Sigma	Cat# D9779; CAS: 3483-12-3
RNasin Recombinant Ribonuclease Inhibitor	Promega	Cat# N2511
SUPERase-in RNase Inhibitor	Thermo Fisher	Cat# AM2694
cOmplete, Mini, EDTA-free Protease Inhibitor Cocktail	Millipore Sigma	Cat# 4693159001
IGEPAL CA-630	Millipore Sigma	Cat# I8896-50ML; CAS: 9002-93-1
07:0 PC DHPC	Avanti Polar Lipids	Cat# 850306P-200 mg; CAS: 39036-04-9
Pierce Recombinant Protein L, Biotinylated	Thermo Fisher	Cat# 29997
Ethanol	Millipore Sigma	Cat# E7023; CAS: 64-17-5
Methanol	Millipore Sigma	Cat# 322415; CAS: 67-56-1

Author Manuscript Author Manuscript Author Manuscript Author Manuscript

REAGENT or RESOURCE	SOURCE	IDENTIFIER
PBS, 10X, RNase-free	Thermo Fisher	Cat# AM9625
Nuclease-free water	Thermo Fisher	Cat# AM9939
Glucose	Millipore Sigma	Cat# G7528; CAS: 50-99-7
HBSS, 10X	Thermo Fisher	Cat# 14065056
HEPES, 1M, pH 7.3, RNase-free	Fisher Scientific	Cat# AAJ16924AE; CAS: 7365-45-9
Magnesium chloride, 1M, RNase-free	Thermo Fisher	Cat# AM9530G; CAS: 7786-30-3
Potassium chloride, 2M, RNase-free	Thermo Fisher	Cat# AM9640G; CAS: 7447-40-7
Sodium azide	Millipore Sigma	Cat# S2002; CAS: 26628-22-8
Sulfolane	Millipore Sigma	Cat# T22209-100G; CAS: 126-33-0
Critical commercial assays		
Vectastain Elite ABC-HRP Kit, Peroxidase (Standard)	Vector Laboratories	PK-6100
DAB Subtrate Kit, Peroxidase (HRP), with Nickel	Vector Laboratories	SK-4100
RNAscope Multiplex Fluorescent V2 Assay	ACD Bio	323100
Absolutely RNA Nanoprep kit	Agilent	400753
Nugen Ovation RNA-Seq System V2	Tecan – NuGEN Technologies	7102-32
TruSeq RNA Library Prep Kit v2	Illumina	RS-122-2001
Dynabeads MyOne Streptavidin T1	Thermo Fisher	65602
Bioanalyzer High Sensitivity RNA 6000 Pico Kit	Agilent	5067-1513
Bioanalyzer High Sensitivity RNA 6000 Nano Kit	Agilent	5067-1511
Deposited data		
Raw and analyzed TRAP RNA-Sequencing data	This paper	GEO: GSE172484
Mouse reference genome UCSC build 10, mm10	UCSC Genomics Institute	https://genome.ucsc.edu/cgi-bin/hgGateway?db=mm10
Custom code	Zenodo	https://doi.org/10.5281/zenodo.6320615
Experimental models: organisms/strains		
Mouse: C57Bl/6J	The Jackson Laboratory	JAX #000664: RRID:IMSR_JAX:000664
Mouse: B6SJL-Tg(SOD1*G93A)1Gur/J	The Jackson Laboratory	JAX #002726: RRID:IMSR_JAX:004435
Mouse: B6.FVB(Cg)-Tg(Colgalt2-EGFP/Rpl10a)DU9Htz/J	The Jackson Laboratory	JAX #030257: RRID:IMSR_JAX:030257
Mouse: B6.FVB(Cg)-Tg(Gprin3-EGFP/Rpl10a)ES152	Eric F. Schmidt	N/A
Mouse: Tg(Gng7-cre)KH67Gsat	GENSAT Project	RRID:MMRRC_031180-UCD
Oligonucleotides		
GFP forward	AAGTTCATCTGCACCACCG	N/A
GFP reverse	TCCTTGAAGAAGATGGTGCG	N/A
SOD1*G93A positive control forward	CACGTGGGCTCCAGCATT	N/A
SOD1*G93A positive control reverse	TCACCAGTCATTTCTGCCTTTG	N/A
SOD1*G93A transgene forward	GGGAAGCTGTTGTCCCAAG	N/A
SOD1*G93A transgene reverse	CAAGGGGAGGTAAAAGAGAGC	N/A
MitoGFP into DIO pAAV forward	TCGTGAGGTACCGGATCCAT GGCGGCCG	N/A

Author Manuscript Author Manuscript Author Manuscript Author Manuscript

REAGENT or RESOURCE	SOURCE	IDENTIFIER
MitoGFP into DIO pAAV reverse	GCTTGATATCGAATTCTTA TGCGTAGTCAGGC	N/A
mCherry-TOMM20 into pAAV forward	TGAGGTACCGGATCCATGGT GGGTCGGAAC	N/A
mCherry-TOMM20 into pAAV reverse	CTTGATATCGAATTCTTACTT GTACAGCTCGTCCATGCC	N/A
Recombinant DNA		
pLYS1-FLAG-MitoGFP-HA	Vamsi Mootha	RRID: Addgene_50057
pAAV-EF1a-DIO-MitoGFP-WPRE-HGHpA	This paper	N/A
CMV-mCherry-TOMM20-N-10	Michael Davidson	RRID: Addgene_55146
pAAV-EF1a-mCherry-TOMM20-WPRE-HGHpA	This paper	N/A
Software and algorithms		
FIJI/ImageJ	Rueden et al. (2017): Schindelin et al. (2012): Schneider et al. (2012)	https://imagej.net/Fiji
MiNA v3.0.1	(Valente et al., 2017)	https://github.com/StuartLab/MiNA
Neurolucida, v11.03	MBF Bioscience	https://www.mbfbioscience.com/neurolucida
Zeiss ZEN	Zeiss	https://www.zeiss.com/microscopy/us/products/microscope-software/zen.html
Rsubread v1.30.6	Liao et al. (2013)	https://bioconductor.org/packages/release/bioc/html/Rsubread.html
rtracklayer v1.40.6	(Lawrence et al., 2009)	https://bioconductor.org/packages/release/bioc/html/rtracklayer.html
RStudio v1.2.5033	RStudio Team	https://www.rstudio.com/
R v3.6.3	R Core Team	https://www.r-project.org/
DESeq2 v1.26.0	Love et al. (2014)	https://bioconductor.org/packages/release/bioc/html/DESeq2.html
Metascape	Zhou et al. (2019)	https://www.metascape.org